Geochemistry of thermal waters in the Southern Volcanic Zone, Chile – Implications for structural controls on geothermal fluid composition

Jackie Wrage[a,b,*], Daniele Tardani[a,b], Martin Reich[a,b], Linda Daniele[a,b], Gloria Arancibia[b,c], José Cembrano[b,c], Pablo Sánchez-Alfaro[a,b], Diego Morata[a,b], Rodrigo Pérez-Moreno[a,b]

[a] Department of Geology, FCFM, Universidad de Chile, Plaza Ercilla 803, Santiago, Chile
[b] Andean Geothermal Center of Excellence (CEGA), FCFM, Universidad de Chile, Santiago, Chile
[c] Department of Structural and Geotechnical Engineering, Pontificia Universidad Católica de Chile, 7820436 Santiago, Chile

ABSTRACT

Thermal waters in the Southern Volcanic Zone (SVZ) of Chile between 36°–41°S were studied using major and selected trace element relationships to characterize their geochemistry, formation mechanisms, and to explore the influence of regional structural controls on fluid composition. Three sets of waters were identified based on physicochemical characteristics: (i) NaCl waters, (ii) acid-sulfate waters, and (iii) bicarbonate (HCO_3) waters. NaCl waters are the most abundant type in the studied region and their chemistry is controlled by significant water-rock interaction. They are characterized by an alkaline pH (7.2–9.3), generally lower temperatures (avg: 55 °C), and relatively high concentrations of Cl, Na, B, As, Li, and Cs. Acid-sulfate waters are typically associated with volcanoes and have a strong magmatic/volcanic component due to the absorption of magmatic vapors. They are acidic (pH < 4), generally higher in temperature (avg: 85 °C), and have elevated concentrations of SO_4, Mg, and Ba. Bicarbonate waters are characterized by the highest concentrations of HCO_3 (> 892 ppm) in the region and are similar in temperature (< 47 °C) and pH (> 6.2) to NaCl waters. They have elevated concentrations of most cations (Ca, K, Na, Mg, Ba, Sr) as a result of intense shallow cation leaching due to the absorption of CO_2-rich volcanic vapors on the peripheries of geothermal systems. The thermal waters were also characterized according to their spatial relation with the dominant fault systems of the region: the NNE-striking intra-arc Liquiñe-Ofqui Fault System (LOFS) and the WNW-striking Andean Transverse Faults (ATF). The inherent differences in fault nature between these fault systems constitutes the primary structural control influencing geothermal fluid development in the SVZ. The chemistry of waters spatially associated with the LOFS as a whole is defined by high vertical permeability networks and lack magmatic reservoir development. Therefore, these waters tend to have higher Cl/B ratios and strong correlations between trace alkali metals and Cl due to rapid, efficient upflow pathways. In contrast, waters spatially associated with the ATF have lower Cl/B ratios and show no correlation between trace alkali metals and Cl due to degassing magma chambers and decreased vertical permeability. The relationship between water type and structural domain in Cl/B ratios and trace metal behavior provides evidence that fault geometry and kinematics exert a fundamental control on geothermal fluid development in the SVZ of Chile.

1. Introduction

Geothermal fluids can have a wide range of dissolved components, modes of formation, and secondary processes influencing their chemistry, all of which act to alter their composition from the reservoir to the surface. Geothermal fluids rising to shallow depths include both hot water and steam with dissolved solutes and gases and the chemical composition and isotope ratios provide important information about the geological, chemical and hydrological characteristics of geothermal systems. Understanding these characteristics is essential for exploration and development of geothermal resources and is also relevant to better understand the formation of epithermal Au-Ag deposits (Arnórsson et al., 2006; Ármannsson, 2009; Kaasalainen et al., 2015; Sánchez-Alfaro et al., 2016a). Mineral precipitation or dissolution, phase separation, meteoric water dilution, depressurization boiling, and vapor condensation all have the potential to enhance or mask chemical signatures of the source fluids during their evolution and ascent (Giggenbach, 1981, 1988; Arnórsson, 1995; Simmons and Browne,

* Corresponding author at: 1565 N 5th St, Laramie, WY, USA.
  E-mail address: jackie.wrage@ndus.edu (J. Wrage).

2000; Arnórsson et al., 2007; Kaasalainen and Stefansson, 2012).

Aquifer fluids commonly have near-neutral to mildly alkaline pH values, with Na, Cl, Si, and CO_2, O_2, H_2, and H_2S being the predominant dissolved solid components and gases (Kaasalainen and Stefansson, 2012). These fluids and vapors may undergo compositional changes near the surface due to vapor condensation or meteoric dilution that produce the various types of geothermal fluid compositions commonly observed in geothermal fields (Allen and Day, 1935; White, 1957; Giggenbach, 1988; Arnórsson, 1995; Arnórsson et al., 2007; Kaasalainen and Stefansson, 2012; Bundschuh and Maity, 2015; Kaasalainen et al., 2015). These include: (i) neutral NaCl waters that likely represent fluids that are well-equilibrated with the host rock in major upflow zones, (ii) steam-heated acid-sulfate waters that result from the absorption of magmatic/volcanic gases in groundwater followed by acid dissolution and alteration of the host rock, (iii) HCO_3 or CO_2-rich waters which are often found at the periphery of hydrothermal systems or around active volcanoes that form through the absorption of CO_2-rich gases of either volcanic or ambient groundwater origin and (iv) mixed waters with variable compositions caused by any combination of the above processes, often dominated by dilution.

The close spatial relationships between tectonic activity, volcanism, and active geothermal systems contribute to shaping the Southern Volcanic Zone (SVZ) of Chile into an outstanding natural laboratory for investigating the interplay of structural controls on the chemical evolution of fluids in geothermal systems. Many studies in the region have focused on the structural controls on isotope signatures (Dobson et al., 2013; Tardani et al., 2016), the link between volcanism and tectonics (Melnick et al., 2006; Rosenau et al., 2006; Cembrano and Lara, 2009; Pérez-Flores et al., 2016), the local effects of fault geometry and kinematics on fluid flow and geochemistry (Sánchez-Alfaro et al., 2013; Roquer et al., 2017), and how structural controls affect mineral precipitation (Sánchez-Alfaro et al., 2016a; Tardani et al., 2017). Despite these recent advances in understanding the relationships between tectonics and fluid flow, there are few studies quantifying these effects on fluid chemistry in thermal waters. Particularly lacking is a comprehensive dataset of elemental concentrations for the entire region and the processes controlling their distribution, speciation and interactions in thermal waters.

Many mechanisms have the potential to alter fluids in geothermal systems to various extents, and the previous structural, kinematic, and magmatic studies on the SVZ provide important constraints to the dominant processes controlling fluid flow. Previous authors have determined that structurally controlled permeability and underlying basement structure are the two most important first-order controls on fluid flow and reservoir development in the SVZ (Cembrano and Lara, 2009; Sánchez-Alfaro et al., 2013; Tardani et al., 2016; Roquer et al., 2017). The goal of this study is to investigate the processes controlling the chemistry of thermal waters in the SVZ by analyzing the geochemistry and relationships of major and selected trace elements to explore the influence of the major structural controls of the region.

2. Geologic and structural setting

The Southern Volcanic Zone (SVZ) is one of the three main segments of the Chilean Andes and extends from 33°S to 46°S along with the Central Volcanic Zone (14°–28°S) and Austral Volcanic Zone (49°–55°S). The region between 36 and 41°S (~ 450 km) is the focus of this study and forms part of the central-southern segment of the SVZ (Fig. 1). Regional tectonics are fundamentally driven by slightly dextral-oblique convergence between the Nazca and South American plates at a rate of about 7–9 cm/year that has prevailed for the last 20 Ma (Pardo-Casas and Molnar, 1987; Somoza, 1998; Angermann et al., 1999).

The regional-scale geology of the SVZ is organized into several margin-parallel belts ranging from Paleozoic plutonic and metamorphic rocks in the Coastal Range to Meso-Cenozoic plutonic and volcano-

sedimentary units in the Main Cordillera (Cembrano and Lara, 2009). The Central Depression, located between the Coastal Range and the Main Cordillera, is characterized by Oligocene to recent volcano-sedimentary rocks (Cembrano and Lara, 2009).

2.1. Regional tectonics

Two regional-scale fault systems are spatially and temporally related to both volcanic and geothermal activity along the SVZ: the arc-parallel Liquiñe-Ofqui Fault System (LOFS) and the Andean Transverse Faults (ATF). The NE- to NNE-striking LOFS and WNW-striking ATF are preferentially oriented and severely misoriented to the prevailing regional stress field, respectively, and therefore exhibit contrasting characteristics in regard to volcanism, fluid circulation, and permeability networks. Fig. 1 details the spatial extent, inferred and mapped traces, and kinematics of the two systems.

The LOFS is a 1200 km-long major intra-arc strike-slip fault system which is defined by master (a series of NNE-striking, subvertical strike-slip faults) and subsidiary faults (steeply dipping, NE-striking normal-dextral faults that splay off master faults) (Cembrano et al., 1996; Lara et al., 2008; Cembrano and Lara, 2009; Pérez-Flores et al., 2016). The LOFS mostly develops extension cracks (EW- to NE-striking), hybrid faults (extension + shear), and pure shear fractures (N to NNE) (Pérez-Flores et al., 2016; Roquer et al., 2017). Architecture of this fault system consists of zones of discrete secondary faults with simple cores and insignificant damage zones or simply individual fault planes (Pérez-Flores et al., 2016; Roquer et al., 2017). The LOFS dominates the SVZ between 38°S and 47°S (Cembrano et al., 1996; Cembrano and Lara, 2009) and constitutes a localized permeability pathway that enhances the vertical migration of fluids due to the existence of transpressional and extensional faults, especially in EW-striking splay faults (Melnick et al., 2006; Sánchez-Alfaro et al., 2013; Held et al., 2016; Pérez-Flores et al., 2016; Tardani et al., 2016; Roquer et al., 2017).

In contrast, the WNW-striking faults of the ATF have been interpreted as crustal weaknesses associated with pre-Andean faults that have been reactivated as sinistral-reverse strike-slip faults during arc development (Cembrano and Moreno, 1994; López-Escobar et al., 1995; Lara et al., 2006; Melnick et al., 2006; Rosenau et al., 2006; Glodny et al., 2008; Lange et al., 2008). The ATF consists of a series of discrete faults that are linked with Quaternary volcanism in the Central and Southern Andes and require high pore fluid pressures or supralithostatic magmatic pressures to become active due to misorientation with respect to the prevailing stress field (Lara et al., 2004, 2006; Cembrano and Lara, 2009; Roquer et al., 2017). Roquer et al. (2017) found that a segment of the ATF records switches in local stress regimes, changing between transpression under the long-term prevailing stress field, which inhibits fluid storage, and transtension when fluid pressures increase up to > 85–98% lithostatic. Architecture of the ATF include multiple cores with very wide damage zones (Pérez-Flores et al., 2016; Roquer et al., 2017).

These fault systems are genetically and spatially related to magmatic evolution in the SVZ, forming two categories of volcano-tectonic associations representing the spatial and temporal affiliation with either the LOFS or the ATF (Cembrano and Moreno, 1994; Lara et al., 2006; Cembrano and Lara, 2009). The subsidiary structures of the LOFS are commonly linked with NE-striking volcanic alignments of stratovolcanoes and/or monogenetic cones, which are directly related to the current bulk dextral transpressional tectonic regime and produce mostly primitive magmas with no magmatic chamber development (Lara et al., 2006; Cembrano and Lara, 2009; Pérez-Flores et al., 2016; Tardani et al., 2016). In addition to influencing the location of volcanic centers, the LOFS is the most significant fault system in directing groundwater flow, which is ultimately responsible for the high concentration of hot springs (35 +) in the central SVZ (Hervé, 1984). In the ATF, the volcanic activity comprises WNW-striking alignments where only stratovolcanoes occur, erupting a wide range of magmatic
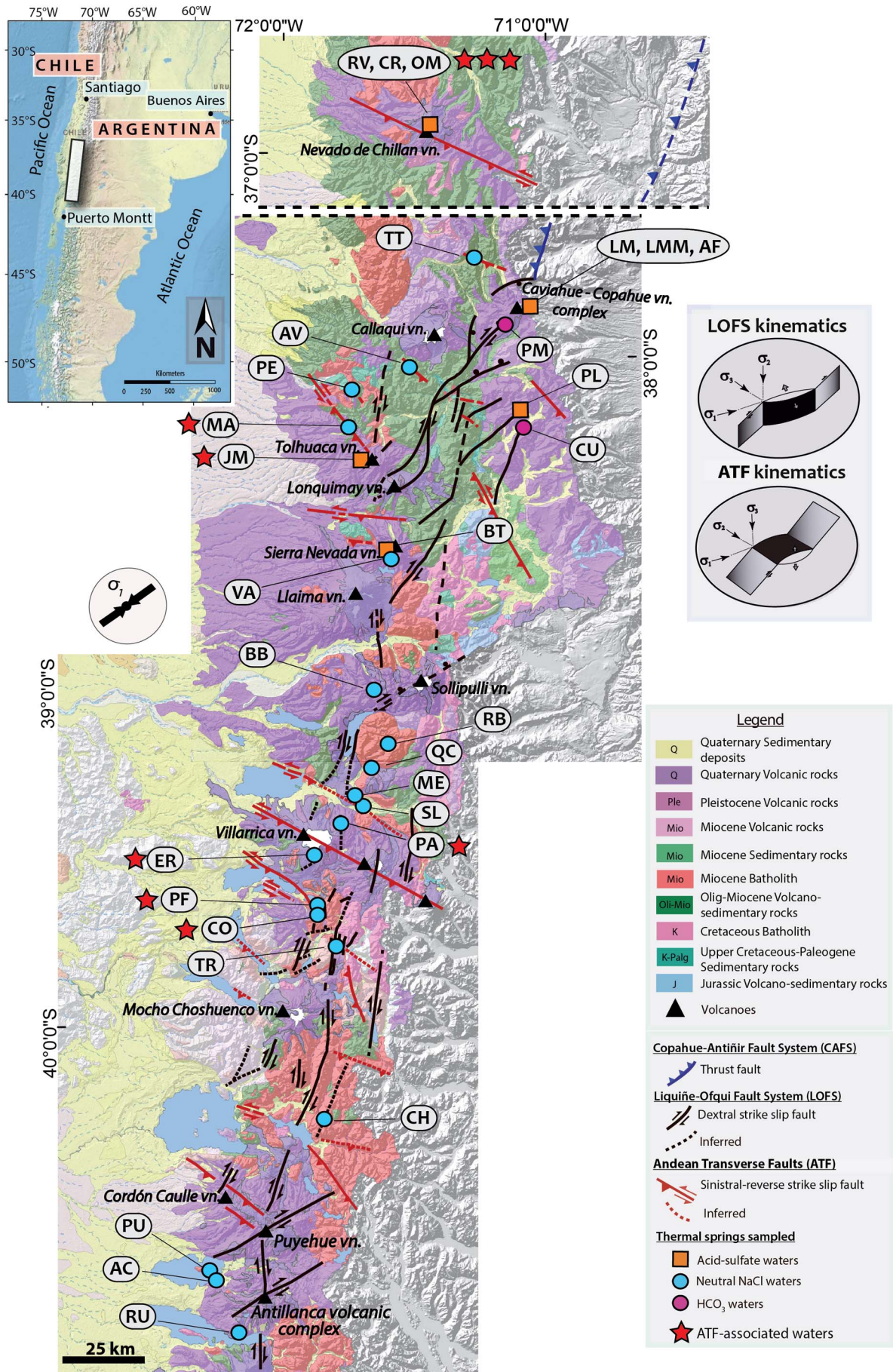
(caption on next page)

Fig. 1. – Map of the studied region showing geology, major fault systems, fault kinematics and extent, and location of sample sites. Samples are displayed based on both water type (shown as data point symbol) and fault association (red star: ATF-associated, no star: LOFS-associated). Modified from Tardani et al. (2016). (For interpretation of the references to colour in this figure legend, the reader is referred to the web version of this article.) (For interpretation of the references to colour in this figure legend, the reader is referred to the web version of this article.)

compositions (basaltic to rhyolitic). The structural elements related to the ATF are suitable for increased magma and hydrothermal migration as well as transient fluid storage under the prevailing transpressional stress regime which promotes long residence times for magma in crustal reservoirs and more evolved magmas (Sánchez-Alfaro et al., 2013; Pérez-Flores et al., 2016; Tardani et al., 2016; Roquer et al., 2017).

2.2. Latitudinal segmentation between 38°and 40°S

The tectonics and fault kinematics of the region between 36° and 41°S have been the subject of many previous studies at different spatial and temporal scales due to the complex interactions between fault systems and existing geological structures (Hervé, 1994; Cembrano et al., 1996; Cembrano, 1998; Lavenu and Cembrano, 1999; Potent and Reuther, 2001; Rosenau et al., 2006; Melnick et al., 2006; Lara et al., 2008; Held et al., 2016; Pérez-Flores et al., 2016; Roquer et al., 2017). There is marked latitudinal segmentation in crustal thickness, upper plate deformation and a changing nature of the basement upon which the volcanic arc has developed in the Chilean Andes (Cembrano and Lara, 2009). In particular, changes in basement geology, exhumation rates, dominant fault systems and subduction-related convergence rates/angles occur within the SVZ between 38° and 40′S (Melnick et al., 2006; Rosenau et al., 2006; Cembrano and Lara, 2009). These changes have the potential to affect magma and fluid migration, development, and residence time in crustal reservoirs by influencing permeability and fault fracture networks (Benavente et al., 2016).

The basement of the SVZ is defined in two distinct geological domains. In the northern domain (33°–37°S) the basement is made up of extensive outcrops of Meso-Cenozoic volcano-sedimentary rocks only locally intruded by Mio-Pliocene plutons (Melnick et al., 2006; Rosenau et al., 2006; Cembrano and Lara, 2009; Benavente et al., 2016; Tardani et al., 2016) whereas in the southern domain (south of 38°S) recent volcanoes are built directly onto Meso-Cenozoic crystalline plutonic rocks of the Patagonian Batholith (Cembrano and Lara, 2009; Held et al., 2016). Crustal thickness beneath the volcanic arc decreases steadily from about 50 km at 33°S to 35 km at 46°S (Tassara and Yáñez, 2003).

The transition between the Central and Patagonian Andes occurs at 38°S. While the Patagonian Andes are characterized by localized deformation along the LOFS, the deformation north of 38°S is dominated by Quaternary shortening and transpressional/transtensional deformation at the northern termination of the LOFS (Melnick et al., 2006). Melnick et al. (2006) and Cembrano and Lara (2009) attribute the arc-orthogonal extension of this area to the merging of the Antiñir-Copahue and Liquiñe-Ofqui fault zones (Fig. 1). The Antiñir-Copahue fault is a compressive thrust system that develops in the back-arc along the Argentinean foothills and extends from 37°50′S northward about 90 km (Ramos and Folguera, 1999; Melnick et al., 2006). The interaction between these two fault systems at the northern termination of the LOFS has led to an accommodation zone characterized by transtensional deformation and individuated by fault splays and graben formation (Melnick et al., 2006; Tardani et al., 2016).

3. Samples and methods

3.1. Sampling and chemical analysis

Thirty samples of thermal water were collected from surface manifestations within the period of 2013–2015 from selected active geothermal systems in the SVZ between 36° and 41°S. In situ temperature and pH measurement techniques used in this study and the ionic

balance computation was done following reported methodologies of Giggenbach and Goguel (1989). Water samples were filtered through a 0.45 μm filter (cellulose acetate) into pre-cleaned high density polythene bottles. Samples for major cation and trace element analysis were collected and acidified with HNO_3 (Merck Suprapur®) 4 N, 1 ml to 100 ml sample.

Anions (Cl^-, SO_4^{2-}) were determined using Ion Chromatography (IC, Dionex ICS 2100) and major cations (Na^+, K^+, Ca^{2+}, and Mg^{2+}) were determined by Atomic Absorption Spectrophotometry (AAS, Perkin-Elmer Pinaacle 900F) at the Andean Geothermal Center of Excellence (CEGA) Laboratories, University of Chile in Santiago, Chile. SiO_2 contents were analyzed by Portable Photometer (Hanna HI96705) and HCO_3^-/CO_3^{2-} contents were analyzed by volumetric titration methods from Giggenbach and Goguel (1989). Concentrations of selected trace elements (Li, Cs, Rb, Ba, Sr, B, As) were analyzed in AC-TLABS laboratories in Canada using High Resolution–Inductively Coupled Plasma–Mass Spectrometry (HR-ICP-MS). The $^{18}O/^{16}O$ and D/H isotopic ratios ($\delta^{18}O$ and δD ‰ V-SMOW) were measured by isotope ratio mass spectrometry at the Laboratoire de Géochimie des Isotopes Stables (Geotop-UQAM), University of Québec in Montréal, Canada. Table 1 details element/species concentrations, detection limits, isotope ratios, and the characterization of each sample based on water type and structural domain.

3.2. Geochemical modelling

The saturation indices of selected minerals was calculated using PHREEQC software and the Lawrence Livermore National Laboratory database, llnl.dat (Parkhurst and Appelo, 2013). The physicochemical parameters for each sample were entered using data from Table 1 and were equilibrated with a general andesite composition in a relatively oxidizing environment (pe = 4). The charge balance was adjusted to redox equilibrium. The acid-sulfate and HCO_3 samples generally had a higher charge imbalance because certain anions (borates, H_2S/HS^-) were not included in the charge balance calculation, as they were not analyzed in the samples. These ions generally play a more important geochemical role in acidic fluids. The results of these waters had a higher percent error (mean percent errors- acid-sulfate: 18.0%; HCO_3: 15.58%; NaCl: 4.85%) and are considered less accurate than the NaCl samples.

4. Results

4.1. Physicochemical parameters and major ion chemistry

Table 1 shows the measured concentrations of the major and trace elements as well as the physicochemical parameters of the thermal waters sampled for this study. In the studied segment of the SVZ, the waters ranged in temperature from 35° to 93 °C, the pH between 2.2 and 9.3, and total dissolved solids between 120 and 3600 ppm. The samples were divided into three groups based on pH and major ion concentrations: (i) acid-sulfate waters, (ii) NaCl waters, and (iii) bicarbonate waters. Of the thirty total samples, nine classified as acid-sulfate waters, nineteen as neutral NaCl waters, and two as HCO_3 waters. Fig. 2 shows a graph of the element concentration ranges comparing the composition of the three water types and Fig. 3 shows the temperature, pH, and total dissolved solids. Fig. 4 compares the ionic composition, which showcases the distinct anionic and cationic chemistries of the water types.

The acid-sulfate waters are characterized by generally higher temperatures (> 68 °C) and pH of < 4. The average temperature of the
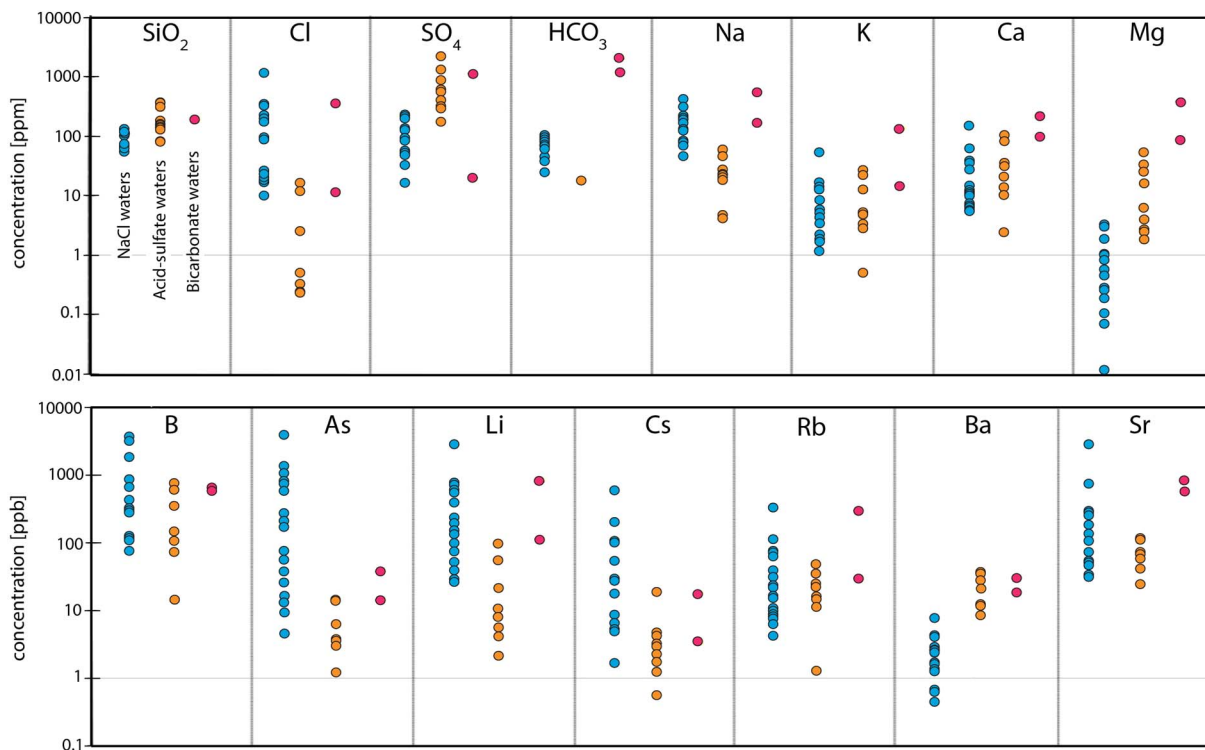
Fig. 2. – Diagram showing the major (top half) and selected trace element (bottom half) concentrations for NaCl waters (blue dots), acid-sulfate waters (orange dots), and HCO₃ waters (pink dots) in the Southern Volcanic Zone of Chile. Units are ppm and ppb for major and trace elements, respectively. (For interpretation of the references to colour in this figure legend, the reader is referred to the web version of this article.) (For interpretation of the references to colour in this figure legend, the reader is referred to the web version of this article.)
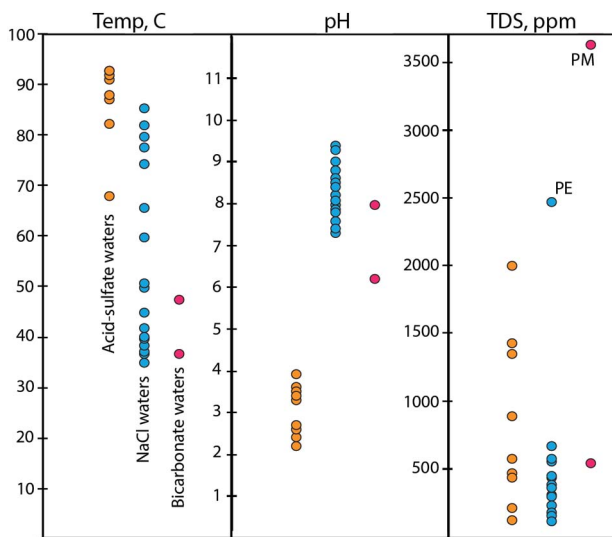

Fig. 3. – Figure showing the temperature, pH, and total dissolved solids (TDS) for the three water types. Samples with anonymously high values are labelled. Symbols are the same as in Fig. 2.

nine samples is 85 °C. They contain relatively high SO_4^{2-} (174–2258 ppm) and low Cl^- (0.22–16.62 ppm) concentrations. Only one sample (RV) contains a measured HCO_3^- concentration (18 ppm HCO_3^-). The nineteen NaCl waters of the study area are characterized by lower temperatures (< 85 °C) and a neutral-alkaline pH ranging from 7.2–9.3. The average temperature is 55 °C. NaCl waters contain much higher concentrations of Cl^- (9.07–876.0 ppm) and HCO_3^- (21.3–88.5 ppm) than acid-sulfate waters and higher relative concentrations of Na, B, As, Li and Cs (Fig. 2). The two bicarbonate water samples are characterized by especially high HCO_3^- concentrations (1550 and 892 ppm), with pH's of 7.9 and 6.2 and temperatures of 47° and 36 °C. While their pH and temperatures are similar to those of NaCl

waters, they contain some of the highest concentrations of dissolved cations (Ca, Mg, Na, K, Sr; Fig. 2).

The anion ternary plot in Fig. 4 shows the relative concentrations of major anions (SO_4^{2-}, Cl^-, HCO_3^-) present in the thermal waters. Acid sulfate waters cluster in the SO_4^{2-} corner while NaCl waters are dispersed throughout the middle of the triangle with broadly similar SO_4/HCO_3 ratios and a wide range in Cl content. Three data points (PE, TT, BB) plot in or close to a mature water composition, defined by Giggenbach (1991) as containing > 60% Cl^- and < 10% SO_4^{2-}. Anionic chemistry is completely dominated by the HCO_3^- species for the bicarbonate water CU while PM is similar in composition to NaCl waters.

4.2. Trace element composition

Trace elements studied in detail for this study include B, As, Li, Cs, Rb, Ba and Sr. The trace alkali metals (Li, Cs, Rb) had concentrations of 2.17–2780 ppb (Li), 0.53–596 ppb (Cs), and 1.29–331 ppb (Rb) as seen in Table 1. Trace alkaline-earth metals (Ba, Sr) are present in the ranges 0.46–43.6 ppb (Ba) and 27.4–2820 ppb (Sr). Lithium and Cs are relatively enriched in NaCl waters whereas Ba is relatively enriched in the acid-sulfate and bicarbonate waters (Fig. 2). Lithium, Rb, and Cs display a strong positive correlation with Cl in the NaCl waters (R^2 close to 1), a weaker positive correlation to Cl in LOFS-associated waters, but no correlation in acid-sulfate waters (Fig. 5). Bicarbonate waters are also displayed in Fig. 5, but no correlations can be drawn from two samples.

The relationships between the relatively conservative alkali metals Li, Rb, and Cs are shown in Fig. 6. Five of the nine acid-sulfate samples plot close to an average crustal rock composition (gray area, lower left). The remaining acid-sulfate, HCO₃ and NaCl samples are generally far from the average composition of the rock, showing a steady depletion in Rb content. NaCl waters and the acid-sulfate samples BT, PL and CR plot near the upflow region of the graph while RV, TT, and RB grade into the outflow region. The two HCO₃ samples do not show the same degree of Rb depletion as the NaCl samples but display a significant depletion in Cs.

Fig. 4. – Piper Diagram comparing the ionic composition of the three water types found in the SVZ. The lower left and right ternary plots show major cation and anion concentrations, respectively, which are then projected onto the diamond. The anion triangle also labels the general fields for immature and mature water compositions after Giggenbach (1991). Data points are labelled with sample ID when practical for viewing purposes.
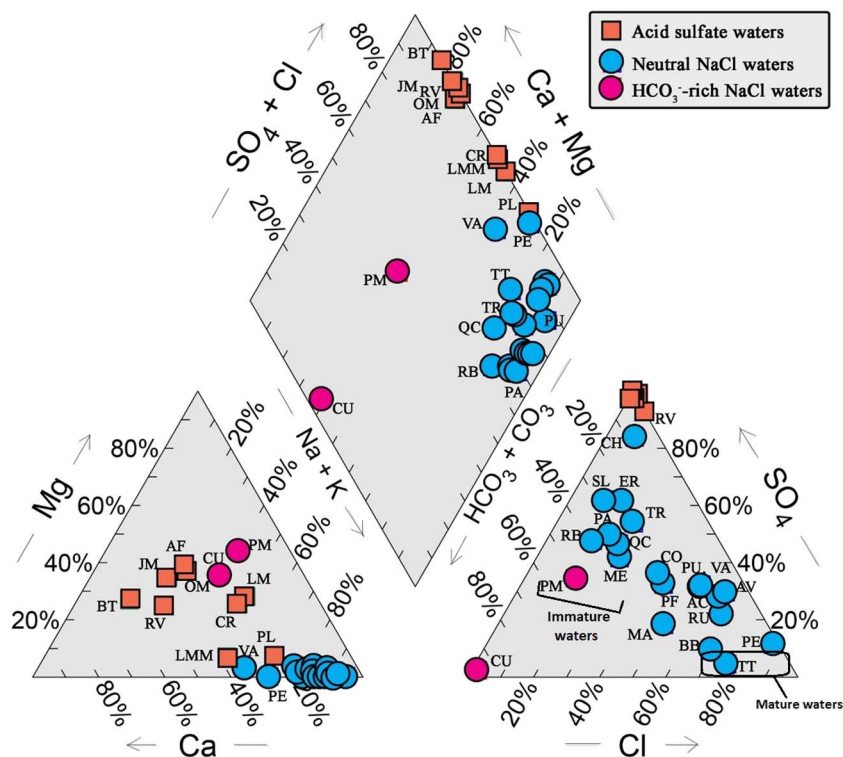
Fig. 7 shows the relative concentrations of Cl, Li, and B. The thermal waters of the SVZ fall into two fields: those waters with lower Cl/B ratios and those with higher Cl/B ratios. No samples plot near an average crustal rock composition (gray area, lower left). Samples CR and OM are the only acid-sulfate waters to show high Cl/B ratios, as the rest are extremely depleted in Cl relative to B. Termas de Malleco (MA) is an NaCl water that also shows this strong depletion in Cl relative to B, plotting with the majority of the acid-sulfate waters. The two bicarbonate waters each lie in a different field, with PM having a high Cl/B ratio and CU having a low Cl/B ratio.

Metalloids (B, As) are present in thermal waters at concentrations between 15.7 and 72,600 ppb (B) and 1.2–3920 ppb (As). Both B and As are enriched in NaCl waters relative to the other two water types, with As showing the highest degree of enrichment (Fig. 2). Six of the NaCl waters (PE, MA, VA, PU, AC, RU, Fig. 1) are B-enriched, with > 10 ppm B (11.2–72.6 ppm). Conversely, all of the B concentrations measured in acid-sulfate and HCO_3 waters are < 1 ppm. Cl and B have a weak positive correlation ($R^2 = 0.68$) in NaCl waters while As and B display a weak positive correlation ($R^2 = 0.65$) in acid-sulfate waters (Fig. 12). The two HCO_3 waters have comparable concentrations of As (14.1 and 36.6 ppb) and B (549 and 644 ppb) but Cl concentrations that differ by an order of magnitude (10.5 and 274 ppm).

4.3. δD and δ¹⁸O isotopic composition

Fig. 8 shows the δD and $\delta^{18}O$ values for the sampled waters of the study area. NaCl-type waters lie close to the global meteoric water line (GMWL), with $\delta^{18}O$ values ranging from − 11.69 to − 8.33 and δD values from − 84.6 to − 53.3. Acid-sulfate-type waters deviate towards isotopic depletion relative to the GMWL on the Andesitic water mixing line, with more variable $\delta^{18}O$ values between − 9.65 and − 0.65 and δD values between − 74.6 and − 43.8. Bicarbonate waters showed similar δD and $\delta^{18}O$ values to NaCl waters ($\delta^{18}O$ = − 11.89 and − 12.4; δD = − 86.8 and − 87.6) and lie close to the GMWL.

5. Discussion

5.1. Geochemical indicators of fluid evolution

Understanding the origin of hydrothermal fluids is an essential step to decipher potential subsurface processes (McCarthy et al., 2005). Using elemental and geochemical relationships along with the general geothermal water formation mechanisms described by Allen and Day (1935), White (1957), Giggenbach (1981, 1988), Arnórsson (1995), Simmons and Browne (2000), Arnórsson et al. (2007) and Kaasalainen and Stefansson (2012), insights into the origin of thermal waters in the studied segment of the SVZ can be unraveled.

5.1.1. Geochemistry of Li, Cs, and Rb: water-rock interaction and elemental uptake by K-bearing minerals

Fig. 9 shows the relationships between the trace alkali metals (Li, Cs, Rb) and B and K, as well as median rock ratios of basalt and rhyolite. When plotted against B (Fig. 9a–c), all but two thermal waters are depleted in metals relative to rock ratios. This suggests either the addition of B by magmatic degassing, preferential release of B during rock leaching, and/or the uptake of Li, Cs, and Rb into alkali-containing minerals (Ellis and Mahon, 1964, 1967; Berger et al., 1988; Shaw and Sturchio, 1992; Kaasalainen and Stefansson, 2012. The interpretations from Fig. 6 suggest the depletions are in part due to the uptake of trace metals into secondary mineral phases in NaCl waters (Cs into zeolites, Rb into K-bearing phases) and to a lesser extent in acid-sulfate and bicarbonate waters.

When plotted against K (Fig. 9d-f), Li and Cs show a higher degree of scatter than Rb when compared to the median rock ratios. Lithium and Cs are less compatible than Rb when substituting for K in minerals due to their larger difference in ion size. NaCl waters consistently plot higher than acid-sulfate waters and initial rock ratios in Fig. 9d and f, indicating an enrichment of Li and Cs relative to K. The high solubility and conservative behavior of Li and the relatively large size of the Cs ion is concurrent with this relative enrichment due to a lower degree of incorporation into secondary minerals compared to K and Rb (Ellis and

Table 1
– Chemical and isotopic compositions of thermal waters from the Southern Volcanic Zone, Chile.

#	ID	Location name	Water type	Fault domain	t °C	pH	TDS (ppm)	SiO₂	Cl	SO₄	HCO₃	Na	K	Ca	Mg
														Major elements, ppm	
						Detection limits (ppm):		0.01	0.01	0.01	0.01	0.005	0.001	0.005	0.0002
1	RV	Nevado de Chillan Vn.	AS	ATF	68.0	3.9	570	370.0	0.25	552.00	18.00	56.00	21.48	105.40	33.10
2	CR	Nevado de Chillan Vn.	AS	ATF	82.0	2.6	440	178.0	16.62	293.76	bd	20.00	4.45	10.00	6.18
3	OM	Nevado de Chillan Vn.	AS	ATF	91.0	2.4	890	290.0	11.82	881.79		58.10	26.60	81.30	52.00
4	TT	Trapa Trapa	NaCl	LOFS	45.0	7.8	550	50.0	178.00	14.40	76.88	134.00	1.70	29.00	3.20
5	AF	Copahue Vn.	AS	LOFS	87.0	2.7	2000	152.0	0.22	2258.00		22.90	12.50	35.50	24.20
6	LMM	Copahue Vn.	AS	LOFS	93.0	3.6	470	310.0	0.32	414.52		27.70	12.40	20.90	2.40
7	LM	Copahue Vn.	AS	LOFS	88.0	2.2	1420	134.0	2.50	1336.19	bd	4.75	2.75	2.34	1.88
8	PM	Pucon Mahuida	HCO₃	LOFS	47.0	7.9	3600	156.0	274.00	841.00	1550.00	440.00	108.00	172.00	294.00
9	AV	Termas del Avellano	NaCl	LOFS	78.0	7.7	430	45.0	273.00	173.00	52.00	246.00	12.30	34.00	0.20
10	PE	Termas de Pemehue	NaCl	LOFS	38.5	7.5	2450	95.0	876.00	155.00	32.00	325.00	45.80	122.00	0.44
11	PL	Pelehue	AS	LOFS	82.0	3.3	120	79.0	0.24	320.00	bd	45.30	3.39	13.90	2.71
12	CU	Termas de Coyuco	HCO₃	LOFS	36.0	6.2	540	156.0	10.50	17.40	892.00	135.00	13.10	82.20	69.50
13	MA	Termas Malleco	NaCl	ATF	85.5	8.4	350	87.6	82.10	40.40	88.50	108.00	4.80	6.68	0.08
14	JM	Tolhuaca Vn.	AS	ATF	92.0	2.4	1340	82.0	0.50	645.00	bd	17.30	5.20	31.40	16.00
15	BT	Sierra Nevada Vn.	AS	LOFS	87.0	3.4	210	120.0	0.22	174.00	bd	4.10	0.50	13.90	3.96
16	VA	Agua de la Vaca	NaCl	LOFS	35.0	7.2	360	84.0	138.00	110.00	56.74	99.10	14.90	52.20	2.98
17	BB	Termas de Balboa	NaCl	LOFS	45.0	7.3	380	110.0	157.00	28.60	84.10	135.00	10.90	13.40	2.70
18	RB	Termas de Rio Blanco	NaCl	LOFS	51.0	7.7	140	53.0	17.10	78.60	80.20	71.80	1.79	10.60	0.46
19	QC	Termas Quimey-Có	NaCl	LOFS	45.0	8.1	120	53.0	15.80	44.40	37.50	39.00	1.09	8.38	0.60
20	ME	Parque Termal Menetúe	NaCl	LOFS	42.0	9.2	160	64.0	22.20	49.70	50.34	64.00	1.16	5.04	0.57
21	SL	Termas de San Luis	NaCl	LOFS	40.0	9.3	300	61.0	9.07	70.60	39.20	60.40	1.11	5.12	0.12
22	PA	Termas de Palguin	NaCl	ATF	50.0	8.9	220	65.0	19.20	72.20	60.03	67.80	2.13	5.65	0.60
23	ER	Termas El Rincón	NaCl	ATF	37.0	7.7	220	84.0	20.20	109.00	50.30	71.70	4.98	10.90	1.77
24	PF	Eco Termas Pellaifa	NaCl	ATF	50.0	8.0	120	63.0	73.40	74.80	71.70	111.00	3.18	6.85	0.28
25	CO	Termas de Coñaripe	NaCl	ATF	74.6	8.5	440	91.0	79.60	98.80	82.40	132.00	3.97	6.15	0.26
26	TR	Termas de Trafipan	NaCl	LOFS	37.2	8.7	170	48.0	23.60	73.20	39.40	57.60	1.61	9.82	0.82
27	CH	Termas de Chihuio	NaCl	LOFS	82.5	9.3	300	90.2	14.40	188.00	21.30	103.00	4.74	13.10	0.01
28	PU	Termas de Puyehue	NaCl	LOFS	60.0	8.3	430	87.0	148.00	116.00	63.46	160.00	5.64	8.78	0.79
29	AC	Termas de Aguas Calientes	NaCl	LOFS	66.0	7.8	560	95.0	191.00	118.00	53.08	179.00	8.00	23.20	1.04
30	RU	Termas de Rupanco	NaCl	LOFS	80.0	7.9	660	109.0	245.00	113.00	78.71	184.00	7.53	23.60	0.30

*bd - below detection limit
*AS - acid-sulfate water

Table 1 (continued)

| #	ID	Location name	Water type	Fault domain	Trace elements, ppb							Isotopes	
					B	As	Li	Cs	Rb	Ba	Sr	$\delta^{18}O$	δ^2H
				Detection limits (ppm):	0.1	0.02	0.05	0.001	0.005	0.01	0.01		
1	RV	Nevado de Chillan Vn.	AS	ATF	440.00	1.20	64.30	3.45	12.20	40.00	78.60	− 9.32	− 68.20
2	GR	Nevado de Chillan Vn.	AS	ATF	15.70	4.07	23.90	4.28	16.10	13.30	47.50	− 9.65	− 74.60
3	OM	Nevado de Chillan Vn.	AS	ATF	88.50	3.05	11.70	2.33	54.30	32.20	143.00	− 6.18	− 51.90
4	TT	Trapa Trapa	NaCl	LOFS	276.00	16.10	74.80	1.66	4.25	1.74	305.00	− 11.69	− 84.60
5	AF	Copahue Vn.	AS	LOFS	82.70	4.06	5.88	1.73	56.90	31.10	141.00	− 4.64	− 56.10
6	LMM	Copahue Vn.	AS	LOFS	450.00	3.46	8.85	5.08	40.30	23.40	87.20	− 0.65	− 51.80
7	LM	Copahue Vn.	AS	LOFS	773.00	15.20	2.17	1.24	24.00	9.19	27.40		
8	PM	Pucon Mahuida	HCO₃	LOFS	549.00	14.10	810.00	17.60	285.00	30.50	816.00	− 11.89	− 86.80
9	AV	Termas del Avellano	NaCl	LOFS	437.00	212.00	691.00	110.00	70.80	2.35	756.00	− 10.90	− 74.10
10	PE	Termas de Pemehue	NaCl	LOFS	17,200.00	3920.00	2780.00	596.00	331.00	7.98	2820.00	− 9.27	− 63.50
11	PL	Pelehue	AS	LOFS	989.30	16.20	119.00	21.30	18.50	12.90	130.00	− 1.88	− 43.80
12	CU	Termas de Coyuco	HCO₃	LOFS	644.00	36.60	110.00	3.34	28.80	18.10	548.00	− 12.40	− 87.60
13	MA	Termas Malleco	NaCl	ATF	72,600.00	4.62	703.00	53.80	39.50	1.38	51.90		
14	JM	Tolhuaca Vn.	AS	ATF	177.00	6.66	11.70	2.96	29.20	13.60	68.10	− 5.34	− 45.70
15	BT	Sierra Nevada Vn.	AS	LOFS	127.00	4.05	4.47	0.53	1.29	43.60	128.00		
16	VA	Agua de la Vaca	NaCl	LOFS	11,400.00	840.00	786.00	206.00	111.00	2.99	297.00	− 9.89	− 70.20
17	BB	Termas de Balboa	NaCl	LOFS	1840.00	169.00	542.00	54.40	62.50	2.54	106.00	− 9.30	− 65.24
18	RB	Termas de Rio Blanco	NaCl	LOFS	115.00	9.21	132.00	5.20	7.05	2.24	278.00	− 10.12	− 69.01
19	QC	Termas Quimey-Có	NaCl	LOFS	103.00	12.90	29.70	4.73	6.24	1.56	110.00	− 9.66	− 68.22
20	ME	Parque Termal Menetúe	NaCl	LOFS	304.00	26.00	131.00	17.60	11.00	0.61	56.90	− 9.43	− 62.80
21	SL	Termas de San Luis	NaCl	LOFS	126.00	16.50	52.10	6.64	7.40	0.69	74.00	− 9.53	− 64.38
22	PA	Termas de Palguin	NaCl	ATF	670.00	76.60	96.20	8.65	9.27	1.79	31.10	− 10.19	− 72.33
23	ER	Termas El Rincón	NaCl	ATF	851.00	56.40	99.70	5.18	21.80	2.60	34.40	− 10.00	− 70.75
24	PF	Eco Termas Pellaifá	NaCl	ATF	3200.00	1070.00	191.00	17.50	16.80	1.23	44.20	− 8.33	− 57.70
25	CO	Termas de Coñaripe	NaCl	ATF	3740.00	1370.00	229.00	27.50	24.50	4.36	56.70	− 8.36	− 58.04
26	TR	Termas de Trafipan	NaCl	LOFS	330.00	38.10	25.90	5.48	8.26	0.46	71.20	− 9.06	− 59.92
27	CH	Termas de Chihuio	NaCl	LOFS	76.00	13.30	39.10	5.40	15.30	7.50	294.00	− 10.39	− 70.60
28	PU	Termas de Puyehue	NaCl	LOFS	16,100.00	724.00	392.00	30.60	31.10	4.12	138.00	− 8.84	− 58.40
29	AC	Termas de Aguas Calientes	NaCl	LOFS	18,000.00	602.00	583.00	102.00	78.10	7.78	251.00	− 8.97	− 53.30
30	RU	Termas de Rupanco	NaCl	LOFS	19,500.00	279.00	152.00	26.40	30.80	7.37	184.00	− 9.04	− 62.00

*AS - acid-sulfate water
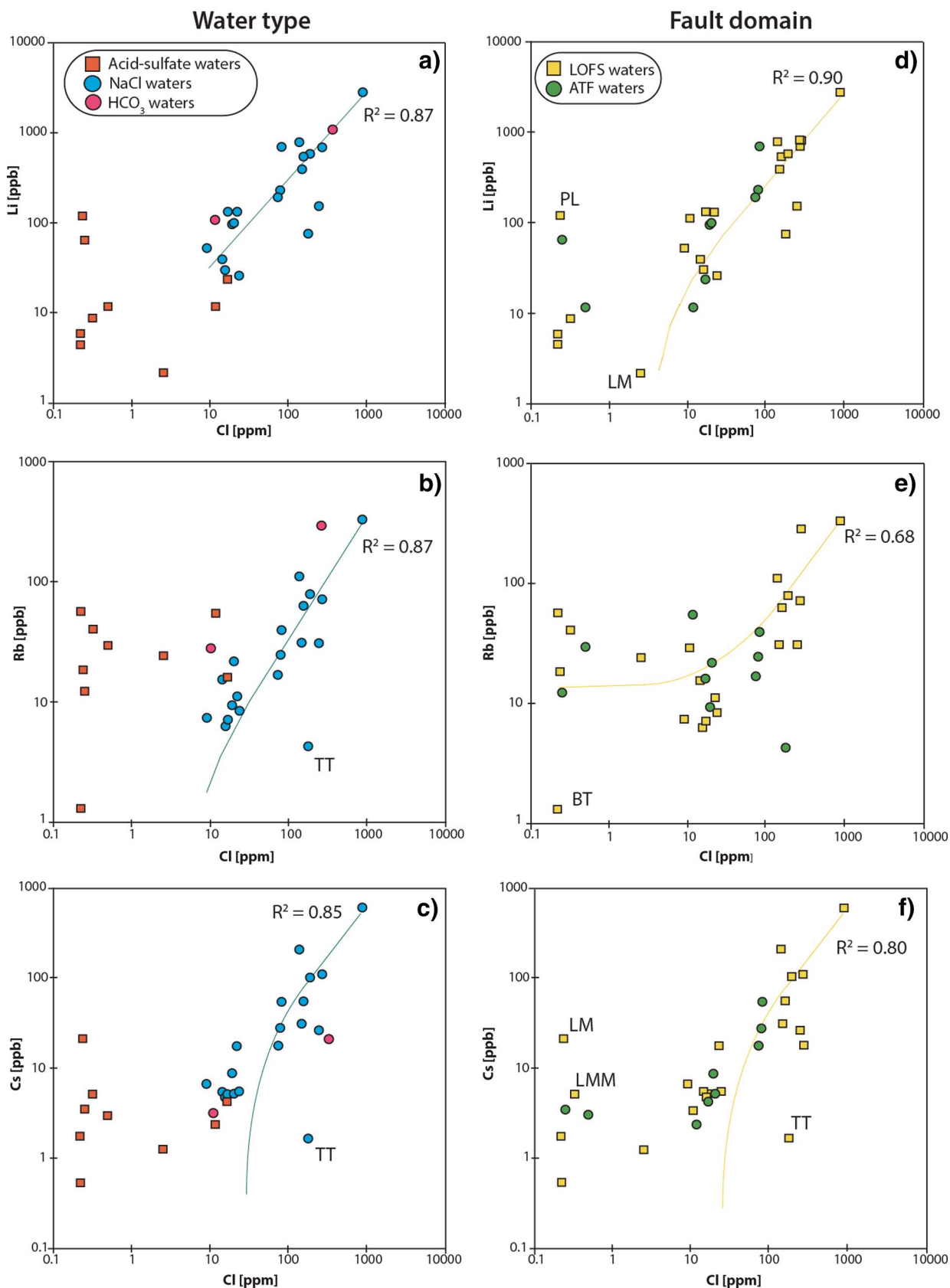
Fig. 5. – Trace alkali metals (Li, Cs, Rb) plotted against Cl concentrations, grouped according to water type (a-c) and spatially associated fault system domain (d-f). Also displayed are the R^2 values for NaCl (a-c) and LOFS (d-f) waters. Outliers are labelled where appropriate. Li, Cs, and Rb have a strong positive correlation with Cl in NaCl and LOFS waters, with R^2 values close to 1, while acid-sulfate and ATF waters show a more scattered distribution ($R^2 < 0.60$).
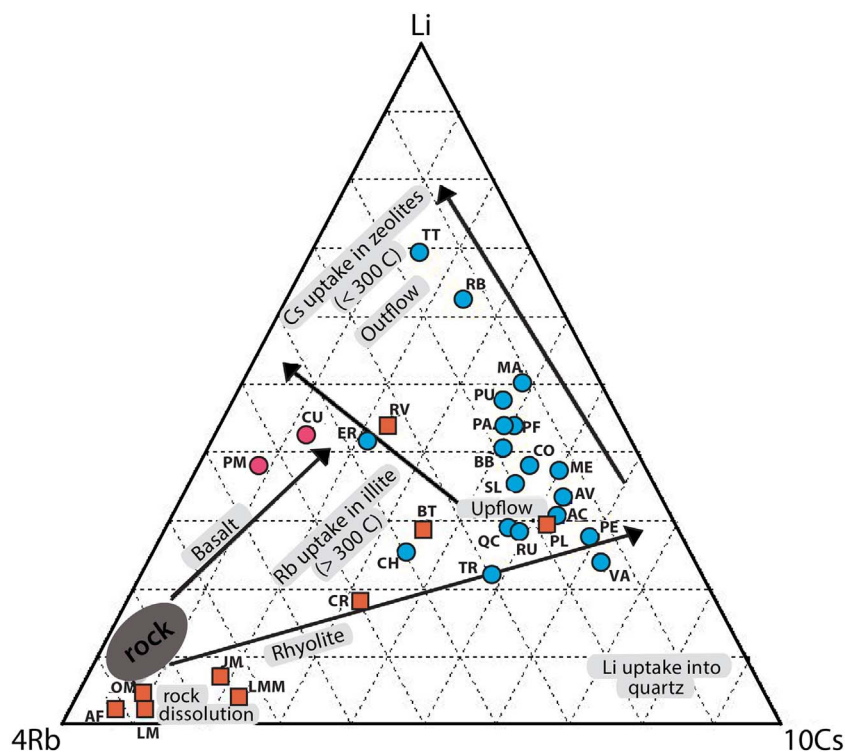
Mahon, 1964, 1967; Goguel, 1983; Sturchio et al., 1986; Kaasalainen and Stefansson, 2012). The strong correlations of these conservative trace metals with Cl in NaCl waters (and to a lesser extent in LOFS waters, Fig. 5) suggests they are sourced from the deep reservoir and transported with Cl to the surface.

Due to the low pH, the geochemistry of the trace alkali metals Li, Rb, and Cs is dominated by rock leaching at depth with minor incorporation into secondary alteration minerals (Fig. 6) in acid-sulfate

waters. In NaCl waters their geochemistry is dominated by aqueous transport as simple cations with Rb- and Cs-incorporation into secondary minerals in the upflow and outflow regions, with Rb showing similar geochemical behavior as K. Alkali trace metal geochemistry in bicarbonate waters appears to be controlled by a combination of the processes described for NaCl and acid-sulfate waters, with Cs-uptake into zeolites also being important (Fig. 6).
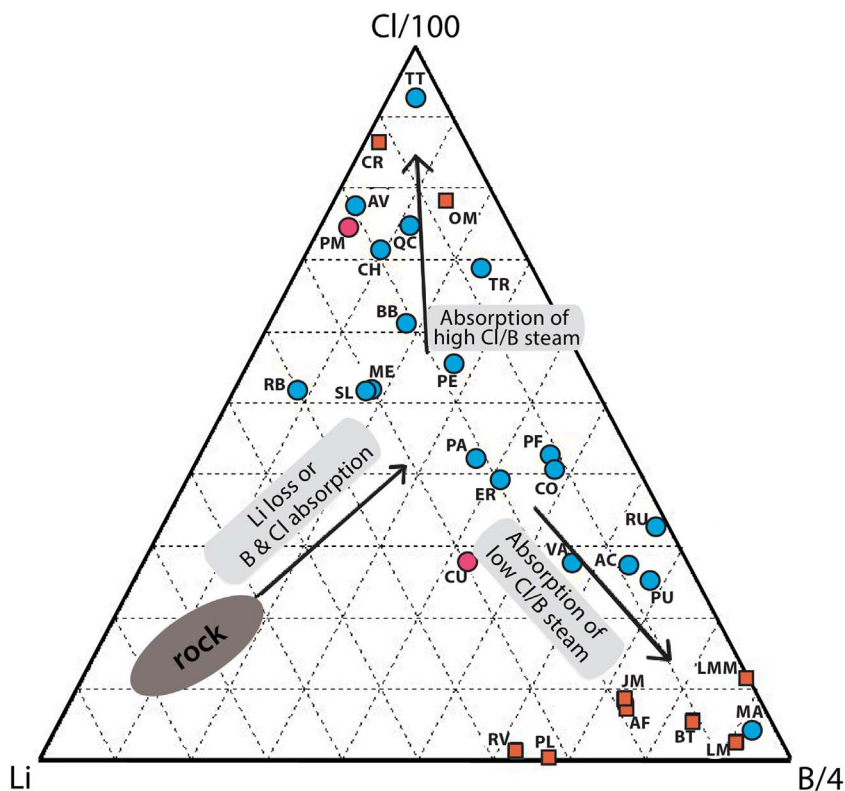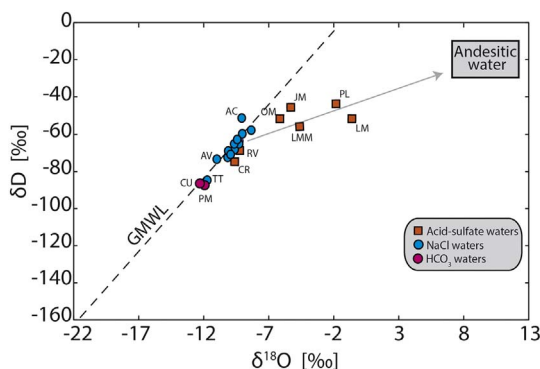
Fig. 8. – δD and δ^{18}O isotopic composition of geothermal fluids of the Southern Volcanic Zone between 36°-41°S. Global meteoric water line (GMWL) and composition of waters in equilibrium with andesitic magmatic fluids are shown. Samples are labelled where possible for readability. Samples AF, MA, and BT are not shown.

5.1.2. Geochemistry of Ba and Sr: rock leaching and carbonate precipitation

The trace alkaline-earth metals Ba and Sr and their relationships to Ca and B are shown in Fig. 10. Both Ba and Sr are depleted relative to median rock ratios when plotted against B (Fig. 10a–b), similar to the trace alkali metals (Fig.9a–c). Acid-sulfate waters generally lie between the median rock ratio lines for both Ba and Sr vs. Ca (Fig. 10c–d) while NaCl waters are slightly depleted in Ba, suggesting relatively stoichiometric behavior between Ba, Sr, and Ca in acid-sulfate waters and a potential sink for Ba in NaCl waters.

Barium and Sr are known to form carbonate and sulfate minerals and to substitute for Ca in various Ca-bearing minerals such as zeolites, carbonates, sulfates or silicates (Kaasalainen and Stefansson, 2012; Kaasalainen et al., 2015). The results of geochemical modelling for Ba- and Sr-bearing mineral phases are shown in Fig. 11. Only pure phases containing Ba and Sr were modelled, but these elements may also replace Ca in alteration minerals (note relationship in Fig. 10d). Carbonate mineral speciation for the acid-sulfate samples is only based on the single sample that had a measured HCO$_3$ content (RV), but the aqueous solution is undersaturated with respect to both minerals for this sample and are expected to become more undersaturated with decreasing pH, which is consistent with the modelling results of Kaasalainen and Stefansson (2012) for carbonate minerals in acid-sulfate waters in Iceland.

While Ba- and Sr-sulfates remained undersaturated in NaCl waters, carbonate minerals approach saturation. These results suggest the precipitation of Ba- and Sr-carbonates could be an effective mechanism of removing these cations from aqueous solution in NaCl waters. Barium is present in much higher concentrations in acid-sulfate waters (acid-sulfate avg. Ba: 24.4 ppb; NaCl avg.: 5.2 ppb). This could be due to a greater degree of rock leaching in acidic acid-sulfate waters while Ba is more effectively removed from solution as witherite or Ca-bearing minerals precipitate in NaCl waters.

The geochemistry of Ba and Sr is strongly controlled by acid rock leaching and potential Ba-sulfate precipitation in acid-sulfate waters. Alkaline water-rock interactions and precipitation of Ba- and Sr-carbonates/Ba-sulfates exert the main control on Ba and Sr geochemistry in NaCl waters.

5.1.3. Geochemistry of As and B: magmatic vapor absorption/As removal and stoichiometric leaching/groundwater mixing

Arsenic and B tend to be correlated with Cl due to volatile behavior at depth (Giroud, 2008), and B and Cl are both considered to be highly mobility in fluids, especially at high temperatures (> 150 °C), due to their incompatibility (Mahon, 1970; Giggenbach, 1991; Arnórsson and Andrésdóttir, 1995; Giroud, 2008). The main sources of B and Cl in thermal waters in the SVZ are most likely magmatic vapors discharged from degassing magma intrusions with minor contributions from local

groundwater/precipitation (Giggenbach, 1991; Arnórsson and Andrésdóttir, 1995; Sánchez-Alfaro et al., 2013). Arsenic is sourced from the leaching of host rocks of geothermal reservoirs and transported to the surface in either the vapor or liquid phase (Giroud, 2008; López et al., 2012; Bundschuh and Maity, 2015).

Fig. 12 shows the Cl versus As (12a) and B (12b) concentrations plotted with seawater and andesite dissolution ratios taken from Giroud (2008) and Purnomo and Pichler (2014). Deep circulation and mixing of meteoric water with geothermal fluids could impart Cl/B concentrations slightly above the andesite dissolution ratio in Fig. 12b. Waters lying along the andesite dissolution line suggests these compositions are controlled primarily by stoichiometric andesitic rock dissolution. The addition of B or loss of Cl lowers the Cl/B ratios and shifts data points below this line, as is observed for many acid-sulfate samples and the NaCl sample MA. The absorption of low Cl/B steam induced by vapor phase separation (discussed in detail in Section 5.1.4) most likely imparted the low Cl/B composition of these waters and is consistent with interpretations from Fig. 7. When As is plotted against B and compared with median rock ratios in Fig. 12c all but one NaCl sample (MA) plots on or near these median rock ratios. Arsenic and B are therefore comparably mobile in nearly all the NaCl-type geothermal fluids of the SVZ, with no significant processes affecting the element concentrations relative to one another. The Termas de Malleco (MA) data point, however, lies far below the rock ratios, as well as two acid-sulfate waters (RV, LMM). Arsenic-uptake into sulfides at depth or co-precipitation onto ferric hydroxides or possibly clays can cause this shift from median rock ratios (Reich et al., 2005; Giroud, 2008; López et al., 2012; Deditius et al., 2014; Kaasalainen et al., 2015).

After interpreting the relationships of As, B, and Cl a few trends can be deduced as to the major processes affecting their concentrations in thermal waters of the SVZ. Waters of the NaCl-type suggest that As and B are controlled by roughly stoichiometric leaching of the host rock at depth, as they lie close to average crustal rock ratios. These elements are influenced mostly by the mixing and dilution of groundwater in NaCl and bicarbonate waters. Acid-sulfate waters, on the other hand, show lower mobility of As relative to B. Rock leaching, uptake/co-precipitation of As in minerals and the absorption of B-enriched magmatic vapors are believed to dominate the geochemistry of these metalloids in acid-sulfate waters due to their high acidity and spatial association with degassing volcanoes.

5.1.4. Origin of acid-sulfate, NaCl, and HCO$_3$ waters in the SVZ

Steam-heated acid-sulfate waters typically form by the mixing of magmatic steam with surface water or steam condensation, which forms by depressurization boiling of aquifer fluids (White, 1957; Giggenbach, 1988; Arnórsson et al., 2007; Kaasalainen and Stefansson, 2012). The steam is rich in volatiles such as H$_2$S and CO$_2$ and can separate from the boiled water to mix and rise through oxygen-rich groundwater. This tends to oxidize H$_2$S to H$_2$SO$_4$, inducing waters with a low pH and intense acid alteration of the rock and soil. This formation mechanism for acid-sulfate waters in the SVZ is consistent with major and selected trace element interpretations, as in Fig. 4 where samples cluster in the SO$_4^{2-}$ corner of the anion triangle. Acid-sulfate waters of the SVZ are also typically discharged by or spatially associated with volcanic systems. This close proximity to a magmatic heat source also implies closeness of the gaseous magmatic components (Arnórsson et al., 2007) necessary for the formation of hot, acid, sulfate-rich thermal waters. The absorption of magmatic vapors into deeply circulating groundwater induces fluid-dominated rock dissolution at depth, preserving conservative element contents in proportions close to those of an average crustal rock and imparting a δD and δ^{18}O signature indicative of magmatic fluid addition. The high degree of Cl depletion in acid-sulfate samples and the weak positive correlation between B and As (R^2 = 0.65) point to the transport of magmatically-derived B and As in these fluids while HCl is depleted in the vapor phase during phase separation (Giggenbach, 1991; Candela, 1994; Pokrovski et al., 2013).
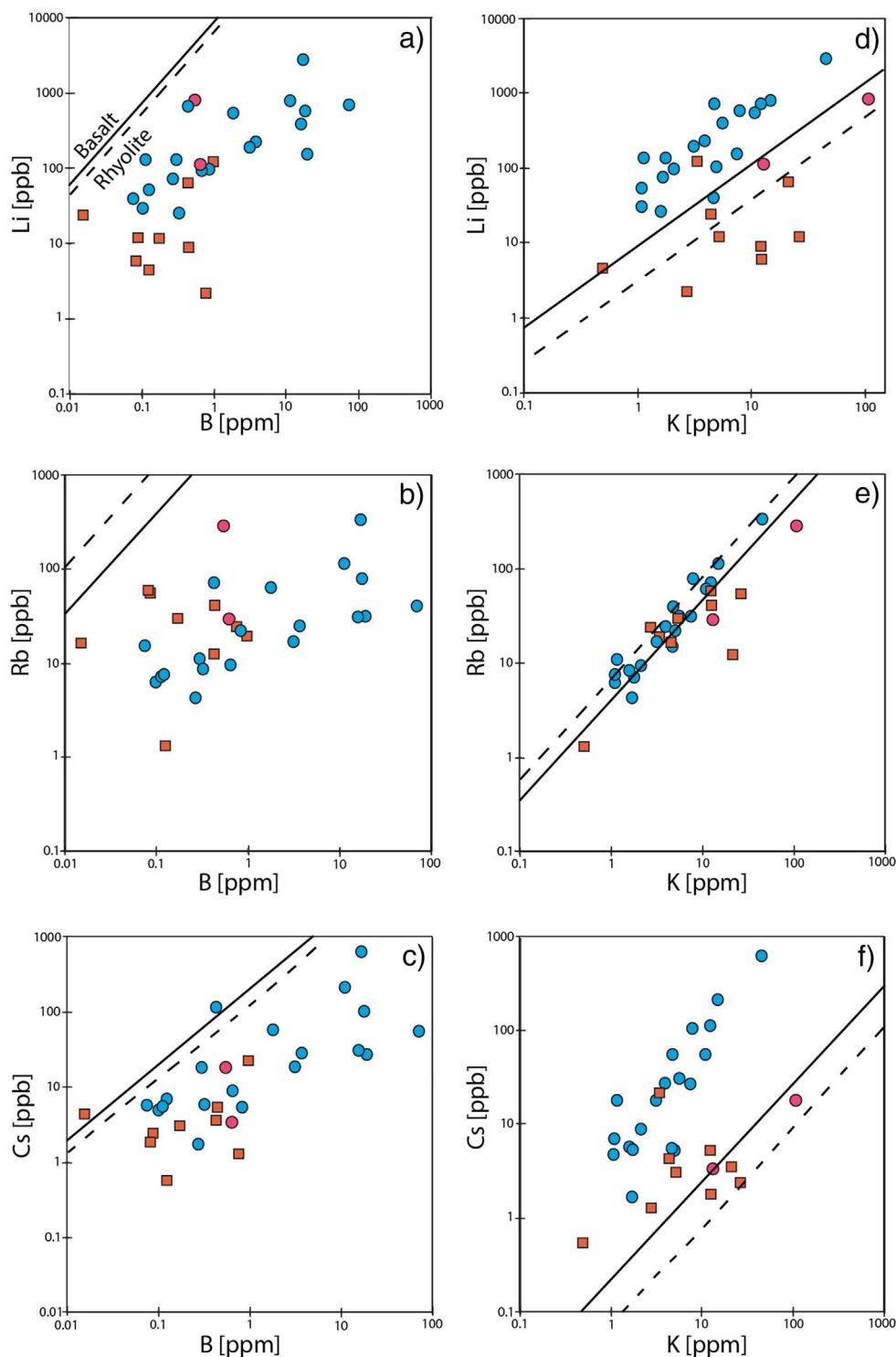
Fig. 9. – Relationships between Li, Cs, and Rb vs. B (a-c) and K(d-f). Also shown are the median rock ratios of basalt (solid line) and rhyolite (dashed line). Graphs modified from Kaasalainen and Stefansson (2012), with the median rock ratios as given by the authors and references therein. Symbols are the same as in Fig. 8.

Based on these data and interpretations, acid-sulfate waters in this segment of the SVZ possess a strong magmatic/volcanic component due to the absorption and circulation of magmatic vapors.

In contrast, typical NaCl waters contain a significant aquifer component and have often undergone depressurization boiling and mixing with shallow ground and surface water in the upflow (Allen and Day, 1935; White, 1957; Giggenbach, 1988; Arnórsson, 1995; Kaasalainen and Stefansson, 2012; López et al., 2012; Bundschuh and Maity, 2015). NaCl waters of the SVZ are commonly discharged by hot springs and represent fluids that have reached varying degrees of maturity due to progressive water-rock interactions in the upflow zone, as evidenced by

the spread of data points in the anion ternary plot in Fig. 4. The strong correlation between trace alkali metals and Cl in NaCl waters is consistent with a fluid that is close in composition to that of the deep aquifer, as once these relatively conservative elements are added to the fluid (especially Li) their concentrations remain virtually unchanged. Overall, NaCl waters have more mature, equilibrated chemistries and reflect significant water-rock interaction in the upflow zone.

Finally, bicarbonate waters are most likely formed through the direct absorption of CO_2 from magmatic steam as it condenses into cool groundwater at the peripheries of volcanic systems (Ellis and Mahon, 1977; Giggenbach, 1993; Simmons and Browne, 2000; Arnórsson et al.,
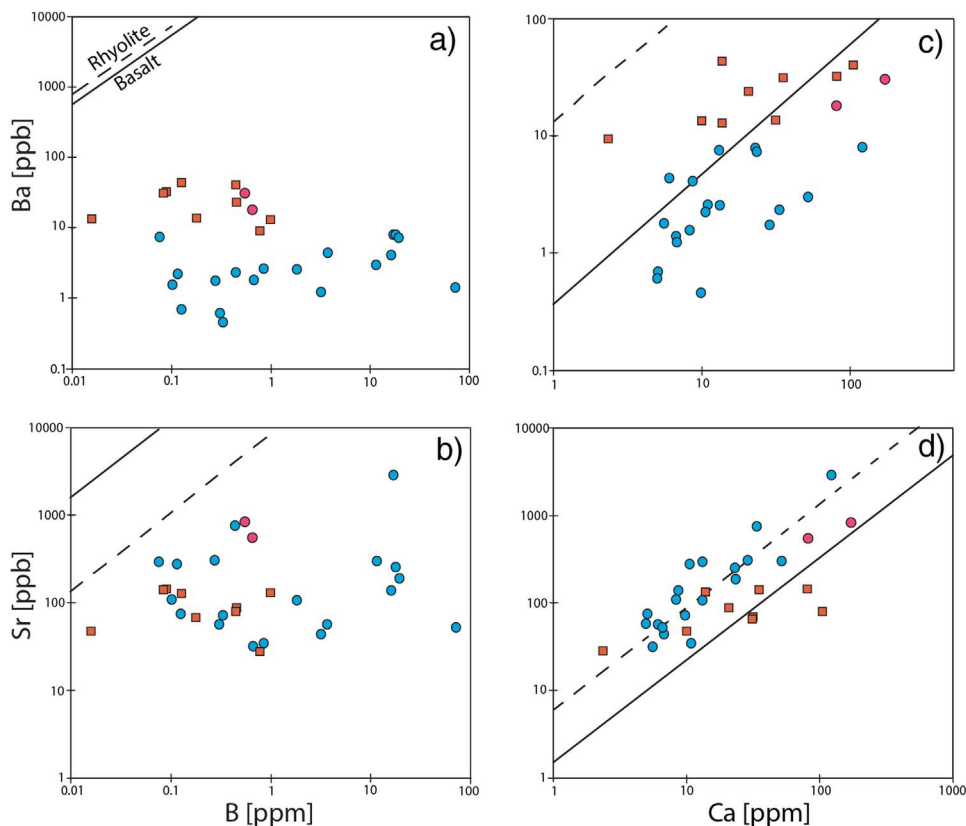
Fig. 10. – Relationships between Ba and Sr vs. B(a-b) and Ca(c-d). Also shown are the median rock ratios of basalt (solid line) and rhyolite (dashed line). Graphs modified from Kaasalainen and Stefansson (2012), with the median rock ratios as given by the authors and references therein. Symbols are the same as in Fig. 8.
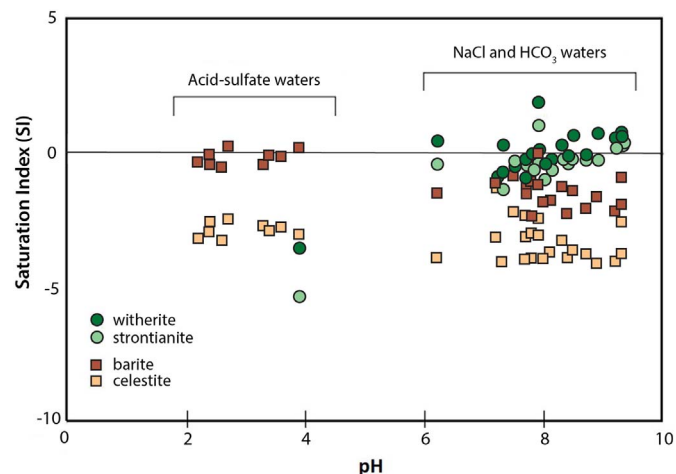

Fig. 11. – Saturation Indices (SI´s) of Ba- and Sr-bearing sulfate (barite & celestite) and carbonate (witherite & strontianite) minerals as a function of water pH. Dotted line indicates SI = 0. Lack of measured carbonate/bicarbonate concentrations in all but one acid sulfate sample is the cause of lack of data points for carbonate minerals in these waters.

2007). This is consistent with $\delta^{13}C$-CO_2 isotope data of Tardani et al. (2016), who concluded that the two HCO_3-rich water locations (CU and PM) were the only samples of the study area affected by hydrothermal degassing, fractionating CO_2 from ^3He and presenting the highest concentration of gaseous CO_2 dissolved in water (97.35% and 99.27%, respectively). These samples also have some of the highest aqueous concentrations of Na, Ca, K, Mg, Ba and Sr in the region (Table 1, Fig. 2). The elevated concentrations of these cations could be due to the primary neutralization process described by Giggenbach (1988), in which the absorption of volcanic gases leads to the formation of a highly reactive acid solution capable of virtually complete cation leaching of the wall rock. This normally occurs deep in the system, but

if the circulation of hydrothermal gases is sufficiently shallow in the presence of circulating groundwater this process could generate the observed elevated cation concentrations. The greater degree of Cs to Rb depletion provides evidence of a peripheral location as Rb uptake into K-bearing minerals occurs at higher temperatures (> 300 °C) while Cs incorporation into zeolites occurs in the lower temperature (< 250 °C) outflow region. Therefore, bicarbonate waters are more of a rarity in the SVZ and reflect hydrothermal degassing at peripheral locations.

5.2. The role of geologic & structural controls on thermal water composition

Structurally controlled permeability and inherited basement geology are the two most important factors controlling fluid flow and reservoir development in the SVZ (Cembrano and Lara, 2009; Sánchez-Alfaro et al., 2013; Held et al., 2016; Tardani et al., 2016; Roquer et al., 2017). The geochemistry of Li, Cs, Rb, Ba, Sr, B and As has been constrained using chemical relationships and geochemical modelling in the previous sections, and these interactions will now be discussed relative to the two dominant geologic and tectonic characteristics of the SVZ to unravel their role in the development of thermal waters.

5.2.1. Effects of basement geology

The basement changes from extensive outcrops of volcano-sedimentary rocks to the plutonic rocks of the Patagonian Batholith south of 38°S in the SVZ. Sánchez-Alfaro et al. (2013) and Rowland and Sibson (2004) provide evidence that in general, fluids in stratified volcanoclastic units favor subhorizontal flow along shallowly plunging folds or bedding planes, which when folded and faulted can hinder the ability of tension cracks from reaching the surface (Sibson, 1996; Cembrano and Lara, 2009). In the local compressional stress regime of the misoriented faults of the ATF, subhorizontal flow could dominate within interconnected subhorizontal reservoirs and the shallowly to deeply-dipping reverse faults as depicted in Fig. 1 for this domain. Conversely, the formation of fault-fracture networks greatly increases vertical permeability within crystalline plutonic rocks, especially under strike-slip
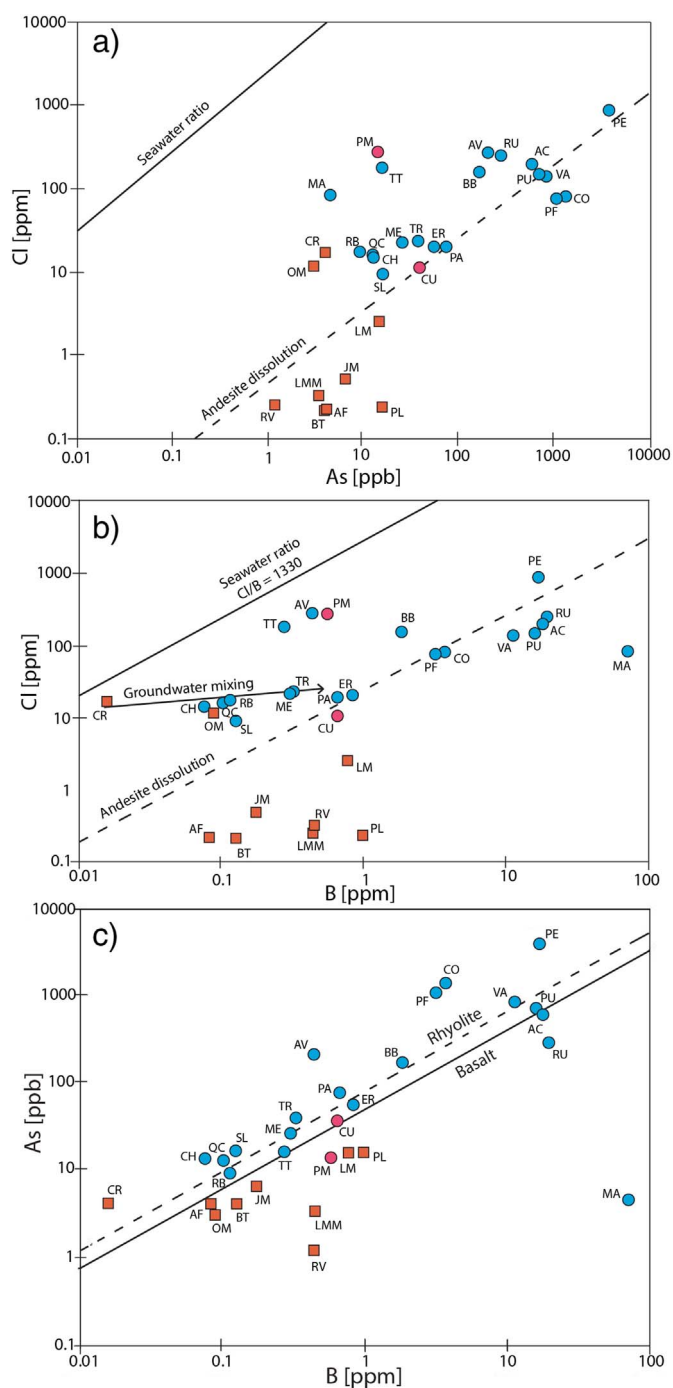
Fig. 12. – Relationships between As and Cl (a), B and Cl (b), and B and As (c). In (a-b) concentrations are shown with seawater ratios and andesite dissolution lines. Fig. 12b also shows groundwater mixing path. Fig. 12c displays the median rock ratios for basalt (solid line) and rhyolite (dashed line). (a) based on Giroud (2008), (b) modified from Purnomo and Pichler (2014), and (c) modified from Kaasalainen and Stefansson (2012). Symbols the same as Fig. 8.

deformation (Rowland and Sibson, 2004; Held et al., 2016). Therefore, in a general sense, fluid pathways north of 38°S are potentially influenced more by subhorizontal flow along bedding planes and within interconnected subhorizontal reservoirs of the ATF while south of 38°S flow is possibly dominated by subvertical fault fracture networks. This difference in fluid flow carries important implications for fluid-rock interactions, upflow zone efficiency and fluid residence time.

The duration of fluid-rock interactions is one of the main factors that governs the state of equilibrium reached in a fluid. The longer a

fluid has to equilibrate with the rock the more mature the chemistry will become (Giggenbach, 1984). Regional or local tectonics may favor such longer residence times in the crust from the geometry of structural meshes formed or reactivated under bulk or local compression, as occurs in the ATF domains. This is not only because overpressure is required to transport fluids along oblique-reverse faults but because the fluid network infrastructure includes subhorizontal cracks in which fluids can be stored for longer periods of time until such fluid overpressure is episodically reached (Roquer et al., 2017).

The anion ternary plot in Fig. 4 depicts the maturity of a fluid based on major anion concentrations. PE, TT, BB, and to a lesser extent RU, AV, AC, VA and PU are the fluids that have reached the highest degrees of maturity in the SVZ. These waters either lie north of 38.57°S (TT, AV, PE, BB, VA) or are the southernmost waters of the study area (PU, AC, RU), as seen in Fig. 1. For waters north of 38.57°S, the subhorizontal flow of fluids and increased water-rock interactions could play a role in imparting a more mature, equilibrated chemistry. TT, AV, PE, BB and VA also lie above the andesite dissolution line in Fig. 12 but are off the groundwater mixing line, suggesting their chemistry is influenced to a greater degree by progressive water-rock equilibrium reactions instead of solely groundwater mixing.

The change in basement geology at 38°S is an important underlying factor to the development of geothermal fluids in the studied segment of the SVZ, potentially exerting a secondary control on the degree of equilibrium reached in thermal fluids within geothermal systems by influencing fluid residence time.

5.2.2. Effects of fault geometry and kinematics

Tectonics of the SVZ are dominated by the NNE- NE-striking LOFS and the WNW-striking ATF, which are two contrasting fault systems that are optimally oriented and severely misoriented to the prevailing stress field, respectively. The geochemical, isotopic and structural data of Tardani et al. (2016) revealed that the degree of crustal contamination is fundamentally controlled by the LOFS and ATF in the Southern Volcanic Zone. As described in Section 2.1, magmas and fluids associated with the LOFS are characterized by a low degree of crustal contamination whereas these fluids are characterized by a higher degree of crustal contamination in the ATF. Fault geometry and kinematics also influence thermal fluid chemistry and behavior (Sánchez-Alfaro et al., 2013; Held et al., 2016; Roquer et al., 2017). Overall, under the prevailing long-term stress conditions, faulting in the LOFS is relatively continuous with cyclic transtension while in the misoriented ATF these conditions facilitate fluid storage. Only until fluid pressures build up to > 85% lithostatic does abnormal transtensional failure occur in the ATF (Roquer et al., 2017).

Tardani et al. (2016) found samples TT, AV, and PE (Fig. 1) to have some of the highest degrees of crustal contamination due to their spatial relationship with transpressional fault-fracture zones that do not permit high vertical permeability. The northern terminus of the LOFS consists of complex extensional and transpressional fault kinematics and is underlain by volcano-sedimentary basement, which could act to increase fluid residence time and decrease local vertical permeability in some areas. This is consistent with the interpretations from the inherited basement geology and water chemistry data of these waters (Section 5.2.1, Table 1). Melnick et al. (2006) proposed that the volcanic activity of the Caviahue-Copahue complex at the northern end of the study area is related to a crustal-scale weakness zone controlled by extensional and transtensional tectonic interactions between the LOFS and the Antiñir-Copahue fault system (Fig. 1). The highly acid waters of the Copahue geothermal area (LM, LMM, AF) are most likely dominated by the "pull apart" transition zone and the large supply of acidifying magmatic vapors released by the underlying magma chamber. This interpretation is supported by Tardani et al. (2016) and Roulleau et al. (2016), who found that the gas and hot springs samples associated with this area showed the most primitive $^3He/^4He$ ratios (Ra = 7.48; 6.16) of the region with no significant degrees of crustal contamination. The two
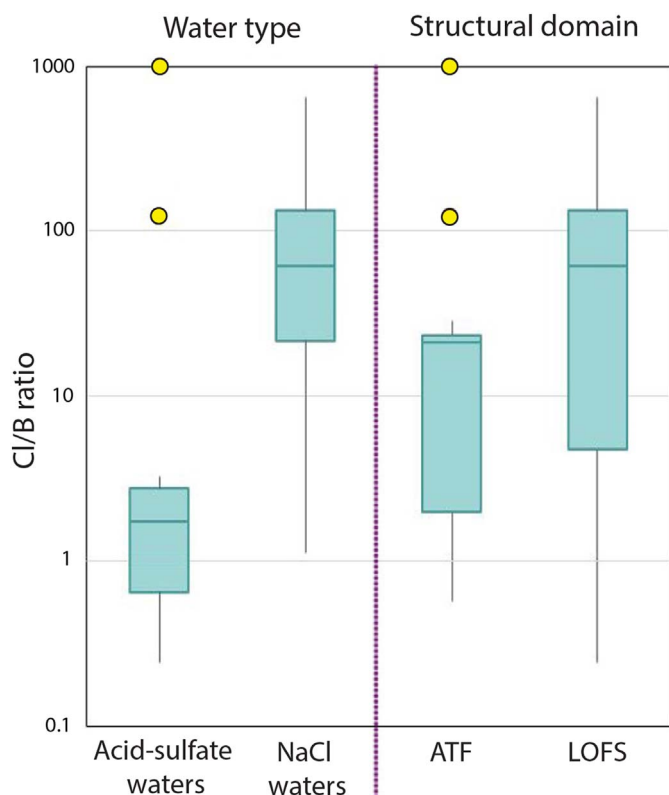
Fig. 13. – Box plot of Cl/B ratios in thermal waters, compared according to water type (acid-sulfate vs NaCl waters, a) and fault domain (LOFS vs ATF, b). The two outliers for acid-sulfate and ATF waters are CR and OM (yellow circles). The two bicarbonate waters are not included in this box plot due to their distinct chemistries. (For interpretation of the references to colour in this figure legend, the reader is referred to the web version of this article.) (For interpretation of the references to colour in this figure legend, the reader is referred to the web version of this article.)

bicarbonate waters are also located in the northern transition zone (Fig. 1). Pucón Mahuida (PM) is located on the southern flank of the Copahue volcano while Termas de Coyuco (CU) is associated with the Pelehue geothermal system about 30 km south. PM and CU do not have similar chemistry to the other thermal waters associated with these geothermal systems, pointing to complex formation mechanisms or distal outflow in these areas.

Fig. 13 is a boxplot of the Cl/B ratios in the study area, where the waters are compared according to both water type and fault association. The acid-sulfate and ATF-associated waters display relatively lower Cl/B ratios while NaCl and LOFS-associated waters show relatively higher ratios. These relationships are in agreement with results obtained by Sánchez-Alfaro et al. (2013) in the Villarrica volcano area of the SVZ, where the authors observed the same relationship between Cl/B ratios in hot springs spatially associated with the two fault domains (ATF – low Cl/B; LOFS – high Cl/B). This relationship suggests that structural controls exert a significant influence on the Cl and B concentrations in thermal waters.

The three northernmost samples (RV, CR, OM) are acid-sulfate waters located at Nevado de Chillán and are entirely controlled by the ATF (Fig. 1). OM and CR are the only acid-sulfate samples with high Cl/B ratios (Figs. 7, 13). These two waters also lie above the andesite dissolution line with most NaCl waters and on the groundwater mixing line in Fig. 12. The third sample in that area (RV), however, falls with the rest of the acid-sulfate samples (Figs. 7, 12, 13). The high degree of scatter (Figs. 6, 7, 8) between these waters that are very closely associated suggests that a simple groundwater mixing and dilution mechanism may not be sufficient to explain the diverse fluid chemistries. The ATF requires high pore fluid pressures to switch the local stress conditions from transpressional to transtensional (Roquer et al., 2017),

which could provide a transient change in fluid chemistry if the fluids stored in the subhorizontal reservoirs were suddenly released. An abrupt change in fluid overpressure conditions has been found to have significant impacts on metal content and fluid chemistry in the Tolhuaca geothermal system, a system in the SVZ that is primarily associated with the ATF (Sánchez-Alfaro et al., 2016b; Tardani et al., 2016, 2017). Therefore, the release of a transient fluid pulse enriched in Cl and depleted in B or a localized area of groundwater mixing/dilution could potentially produce the high Cl/B ratios in thermal waters of Nevado de Chillán or other systems spatially related with the ATF, imparting diverse fluid chemistries within the same local area.

Sample MA (Termas de Malleco) is an NaCl water that is spatially related to the ATF, located NW of the Tolhuaca Volcano and sample JM (Fig. 1). This fluid has an alkaline pH (8.4) and the highest temperature and HCO_3 concentration for NaCl waters (85.5 °C; 88.5 ppm). Boron content is the highest in the region at 72.6 ppm, and shows the greatest degree of B-enrichment relative to rock ratios of all samples (Fig. 10a–b, 12). MA plots far in the region of absorption of low Cl/B steam (Fig. 7), suggesting that this enrichment is a result of its close proximity to a magmatic source (Tolhuaca Volcano, Fig. 1) and the absorption of magmatic vapors rich in B. The exotic chemistry of sample MA provides further evidence of structural controls playing an important role in the development of fluid chemistry in geothermal systems of the SVZ.

The contrasting permeability and magmatic characteristics of the two tectonic domains and the implications they carry for geothermal fluid development can have a direct influence on fluid chemistries. The lower Cl/B ratios of the ATF domain, some of which are characterized as NaCl waters (MA, PA, ER, PF, CO, Fig. 1), are appropriate given the greater degree of magmatic development and subsequent degassing that characterizes systems of the ATF. Decreased vertical permeability and basement geology can also influence water-rock interaction time and can potentially impart a more mature chemical signature (TT, AV, PE). On the other hand, PL and BT, acid-sulfate waters spatially associated with the LOFS, plot near the upflow region in Fig. 6. This suggests these waters had a more efficient pathway to the surface facilitated by the increased vertical permeability of the LOFS system.

6. Summary and concluding remarks

The major and selected trace element chemistry (Li, Cs, Rb, Ba, Sr, As, B) of thermal waters was examined to determine the main processes influencing their formation and geochemistry and to unravel the interplay between these processes and the major structural mechanisms of the SVZ between 36 and 41°S. Based on element behavior and relationships, inherent structurally controlled differences in the two dominant fault systems (LOFS and ATF) were found to play an important role in geothermal fluid development in the studied segment of the SVZ. The ATF-associated waters feature lower Cl/B ratios and no correlation exists between trace alkali metals and Cl. These observations are consistent with the greater degree of magmatic chamber development and degassing as well as geometric misorientation of the NW-striking ATF systems. The waters spatially associated with the LOFS have higher Cl/B ratios due to mixing with meteoric water and lack of magmatic vapor addition. These waters also feature a strong correlation between trace alkali metals and Cl. These characteristics are consistent with the high vertical permeability networks that promote efficient upflow and meteoric mixing that delineate systems of the LOFS, as well as the lack of magmatic chamber development and degassing.

Geothermal systems have been largely understudied in the Andean region, and in particular there is limited scientific information about the role of local kinematic conditions on fluid flow and mineralization during the development and evolution of geothermal reservoirs. Therefore, the results from this study increase our knowledge about structurally controlled geothermal systems in southern Chile, and particularly, provide new insights about the effects of both regional and local tectonics on fluid flow and permeability. The studied region has

some of the greatest geothermal potential for power generation within Central Chile (Sanchez-Alfaro et al., 2015). Thus, and because of its proximity to the Chilean Central Interconnected system (SIC, Sistema Interconectado Central), results generated by this study may directly impact developing exploration strategies to identify promising areas for exploitation of geothermal resources.

Acknowledgements

References

Allen, E., Day, A., 1935. Hot Springs of the Yellowstone National Park. Carnegie Inst. Wash. Publ. 466.

Angermann, D., Klotz, J., Reigber, C., 1999. Space-geodetic estimation of the Nazca-south American Euler vector. Earth Planet. Sci. Lett. 171 (3), 329–334.

Ármannsson, H., 2009. Application of geochemical methods in geothermal exploration. Exploration for Geotherm. (Resour., Kenya, November 1–22).

Arnórsson, S., 1995. Geothermal systems in Iceland: structure and conceptual models 1. High-temperature area. Geothermics 24, 561–602.

Arnórsson, S., Andrésdóttir, A., 1995. Processes controlling the distribution of boron and chlorine in natural waters in Iceland. Geochim. Cosmochim. Acta 59, 4125–4146.

Arnórsson, S., Bjarnason, J., Giroud, N., Gunnarsson, I., Stefánsson, A., 2006. Sampling and analysis of geothermal fluids. Geofluids 6, 203–216.

Arnórsson, S., Stefánsson, A., Bjarnason, J., 2007. Fluid-fluid interactions in geothermal systems. Rev. Mineral. Geochem. 65, 259–312.

Benavente, O., Tassi, F., Reich, M., Aguilera, F., Capechhiacci, F., Gutiérrez, F., Vaselli, O., Rizzo, O., 2016. Chemical and isotopic features of cold and thermal fluids discharged in the Southern Volcanic Zone between 32.5°S and 36°S: insights into the physical and chemical processes controlling fluid geochemistry in geothermal systems of Central Chile. Chem. Geol. 420, 97–113.

Berger, G., Schott, J., Guy, C., 1988. Behavior of Li, Rb, and Cs during basalt glass and olivine dissolution and chlorite, smectite and zeolite precipitation from seawater:-experimental investigations and modelization between 50 °C and 300 °C. Chem. Geol. 297–312.

Bundschuh, J., Maity, J., 2015. Geothermal arsenic: occurrence, mobility and environmental implications. Renew. Sust. Energ. Rev. 42, 1214–1222.

Candela, P., 1994. Combined chemical and physical model for plutonic devolatilization: a non-Rayleigh fractionation algorithm. Geochim. Cosmochim. Acta 58, 2157–2167.

Cembrano, J., 1998. Kinematics and Timing of Intra-arc Deformation at the Southern Andes Plate Boundary Zone. University of Dalhousie (PhD thesis).

Cembrano, J., Lara, L., 2009. The link between volcanism and tectonics in the southern volcanic zone of the Chilean Andes: a review. Tectonophysics 471, 96–113.

Cembrano, J., Moreno, H., 1994. Geometría y naturaleza constrastante del volcanismo cuaternario entre los 38°S y 46°S: ¿Dominios compresionales y tensionales en un régimen transcurrente? In: Proc. Chilean Geol. pp. 240–244 (Congress, 7th, 1).

Cembrano, J., Hervé, F., Lavenu, A., 1996. The Liquiñe-Ofqui fault zone: a long-lived intra-arc fault system in southern Chile. Tectonophysics 259, 55–66.

Deditius, A., Reich, M., Kesler, S., Utsunomiya, S., Chryssoulis, S., Walshe, J., Hough, R., Ewing, R., 2014. The coupled geochemistry of Au and As in pyrite from hydrothermal ore deposits. Geochim. Cosmochim. Acta 140, 644–670.

Dobson, P., Kennedy, B., Reich, M., Sánchez, P., Morata, D., 2013. Effects of volcanism, crustal thickness and large scale faulting on the He isotope signatures of geothermal systems in Chile. In: Thirty-eighth Workshop on Geotherm. Reserv. Eng. Stanford University, Stanford, California (February 11–13, 2013, SGP-TR-198).

Ellis, A., Mahon, W., 1964. Natural hydrothermal systems and experimental hot water/ rock interactions. Geochim. Cosmochim. Acta 28, 1323–1357.

Ellis, A., Mahon, W., 1967. Natural hydrothermal systems and experimental hot water/ rock interactions. Part II. Geochim. Cosmochim. Acta 31, 519–538.

Ellis, A., Mahon, W., 1977. Chemistry and Geothermal Systems. Academic Press.

Giggenbach, W., 1981. Geothermal mineral equilibria. Geochim. Cosmochim. Acta 45, 393–410.

Giggenbach, W., 1984. Mass transfer in hydrothermal alteration systems. Geochim. Cosmochim. Acta 48, 2693–2711.

Giggenbach, W., 1988. Geothermal solute equilibria — derivation of Na-K-Mg-Ca geoindicators. Geochim. Cosmochim. Acta 52, 2749–2765.

Giggenbach, W., 1991. Chemical techniques in geothermal exploration. In: D'Amore, F. (Ed.), Application of Geochemistry in Geothermal Reservoir Development. UNITAR/ UNDP Centre on small energy resources, Rome, Italy.

Giggenbach, W., 1993. Redox control of gas compositions in Philippine volcanic-hydro-thermal systems. Geothermics 22, 575–587.

Giggenbach, W., Goguel, R., 1989. Collection and Analysis of Geothermal and Volcanic Water and Gas Samples. Vol. 2401 Department of Scientific and Industrial Research, Chemistry Division (Report).

Giroud, N., 2008. A Chemical Study of Arsenic, Boron and Gases in High-temperature Geothermal Fluids in Iceland [PhD Thesis]. University of Iceland.

Glodny, J., Echtler, H., Collao, S., Ardiles, M., Burón, P., Figueroa, O., 2008. Differential late Paleozoic active margin evolution in south-Central Chile (37°S–40°S) – the Lanalhue fault zone. J. S. Am. Earth Sci. 26, 394–411.

Goguel, R., 1983. The rare alkalies in hydrothermal alteration at Wairakei and Broadlands, geothermal fields. N. Z. Geochim. et Cosmochim. Acta 47, 429–437.

Held, S., Schill, E., Pavez, M., Diaz, D., Munoz, G., Morata, D., Kohl, T., 2016. Reistivity distribution from mid-crustal conductor to near-surface across the 1200 km long Liquiñe-Ofqui fault system, southern Chile. Geophys. J. Int. 207, 1387–1400.

Hervé, M., 1984. La zona de falla Liquiñe-Ofqui, en Liquiñe. Comunicaciones 34, 107–115.

Hervé, F., 1994. The southern Andes between 39° and 44°S latitude: the geological signature of a transpressive tectonic regime related to a magmatic arc. In: Reutter, K., Scheuber, E., Wigger, P. (Eds.), Tectonics of the Southern Central Andes. Springer, Berline, pp. 243–248.

Kaasalainen, H., Stefansson, A., 2012. The chemistry of trace elements in surface geothermal waters and steam, Iceland. Chem. Geol. 330-331, 60–85.

Kaasalainen, H., Stefansson, A., Giroud, N., Arnorsson, S., 2015. The geochemistry of trace elements in geothermal fluids, Iceland. Appl. Geochem. 62, 207–223.

Lange, D., Cembrano, J., Rietbrock, A., Haberland, C., Dahm, T., Bataille, K., 2008. First seismic record for intra-arc strike-slip tectonics along the Liquiñe-Ofqui fault zone at the obliquely convergent plate margin of the southern Andes. Tectonophysics 455, 14–24.

Lara, L., Naranjo, J., Moreno, H., 2004. Lanín volcano (39.5°S), southern Andes: geology and morphostructural evolution. Rev. Geol. Chile 31 (2), 241–257.

Lara, L., Lavenu, A., Cembrano, J., Rodríguez, C., 2006. Structural controls of volcanism in transversal chains: resheared faults and neotectonics in the Cordón Caulle-Puyehue area (40.5°S, southern Andes). J. Volcanol. Geotherm. Res. 158, 70–86.

Lara, L., Cembrano, J., Lavenu, A., 2008. Quaternary vertical displacement along the Liquiñe-Ofqui fault zone: differential uplift and coeval volcanism in the southern Andes? Int. Geol. Rev. 50, 975–993.

Lavenu, A., Cembrano, J., 1999. Compressional- and transpressional-stress pattern for Pliocene and quaternary brittle deformation in fore arc and intra-arc zones (Andes of central and southern Chile). J. Struct. Geol. 21, 1669–1691.

López, D., Bunchschuh, J., Birkle, P., Armienta, M., Cumbal, L., Sracek, O., Cornejo, L., Ormachea, M., 2012. Arsenic in volcanic geothermal fluids in Latin America. Sci. Environ. 429, 57–75.

López-Escobar, L., Cembrano, J., Moreno, H., 1995. Geochemistry and tectonics of the Chilean southern Andes basaltic quaternary volcanism (37–46°S). Rev. Geol. Chile 22, 219–234.

Mahon, W., 1970. Chemistry in the exploration and exploitation of hydrothermal systems. Geothermics 2, 1310–1322.

McCarthy, K.T., Pichler, T., Price, R.E., 2005. Geochemistry of champagne Hot Springs shallow hydrothermal vent field and associated sediments, Dominica, lesser Antilles. Chem. Geol. 224, 55–68.

Melnick, D., Folguera, A., Ramos, V., 2006. Structural control on arc volcanism: the Caviahue-Copahue complex, central to Patagonian Andes transition (38°S). J. S. Am. Earth Sci. 22, 66–88.

Pardo-Casas, F., Molnar, P., 1987. Relative motion of the Nazca (Farallón) and south American plates since late cretaceous times. Tectonics 6, 233–248.

Parkhurst, D., Appelo, C., 2013. Description of Input and Examples for PHREEQC Version 3—A Computer Program for Speciation, Batch-Reaction, One-Dimensional Transport, and Inverse Geochemical Calculations: U.S. Geological Survey Techniques and Methods, Book 6, Chap. A43. (497 p., available only at). http://pubs.usgs.gov/tm/06/a43/.

Pérez-Flores, P., Cembrano, J., Sánchez-Alfaro, P., Veloso, E., Arancibia, G., Roquer, T., 2016. Tectonics, magmatism and paleo-fluid distribution in a strike-slip setting: insights from the northern termination of the Liquiñe-Ofqui fault system, Chile. Tectonophysics 680, 192–210.

Pokrovski, G., Borisova, A., Bychkov, A., 2013. Speciation and transport of metals and metalloids in geological vapors. Rev. Mineral. Geochem. 76, 165–218.

Potent, S., Reuther, C., 2001. Neogene Deformations prozesse im aktiven magmatischem Bogen Sudzentralchiles zwischen 37° und 39°S. Mitt. Geol.-Palaeontol. Inst. Univ. Hamburg 85, 1–22.

Purnomo, B., Pichler, T., 2014. Geothermal systems on the island of java, Indonesia. J. Volcanol. Geotherm. Res. 285, 47–59.

Ramos, V., Folguera, A., 1999. The Andes of Neuquén (36°-38°S): Evidence of Cenozoic Transtension along the arc. IV Andean Geodynamic Symposium (Gottingen), Extended Abstracts. pp. 606–609.

Reich, M., Kesler, S.E., Utsunomiya, S., Palenik, C.S., Chryssoulis, S., Ewing, R.C., 2005. Solubility of gold in arsenian pyrite. Geochim. Cosmochim. Acta 69, 2781–2796.

Roquer, T., Arancibia, G., Rowland, J., Iturrieta, P., Morata, D., Cembrano, J., 2017. Fault-controlled development of shallow hydrothermal systems: structural and mineralogical insights from the southern Andes. Geothermics 66, 156–173.

Rosenau, M., Melnick, D., Echtler, H., 2006. Kinematic constraints on intra-arc shear and strain partitioning in the southern Andes between 38°S and 42°S latitude. Tectonics 25, 1–16.

Roulleau, E., Tardani, D., Sano, Y., Takahata, N., Vinet, N., Bravo, F., Muñoz, C., Sanchez, J., 2016. New insight from noble gas and stable isotopes of geothermal/hydrothermal fluids at Caviahue-Copahue Volcanic Complex: boiling steam separation and water-rock interaction at shallow depth. J. Volcanol. Geotherm. Res. 328, 70–83.

Rowland, J., Sibson, R., 2004. Structural controls on hydrothermal flow in a segmented rift system, Taupo volcanic zone, New Zealand. Geofluids 4 (4), 259–283.

Sánchez-Alfaro, P., Pérez-Flores, P., Arancibia, G., Cembrano, J., Reich, M., 2013. Crustal deformation effects on the chemical evolution of geothermal systems: the intra-arc

Liquiñe-Ofqui fault system, southern Andes. Int. Geol. Rev. 55, 1384–1400.

Sanchez-Alfaro, P., Sielfeld, G., Van Campen, B., Dobson, P., Fuentes, V., Reed, A., Palma-Behnke, R., Morata, D., 2015. Geothermal barriers, policies and economics in Chile – lessons for the Andes. Renew. Sust. Energ. Rev. 51, 1390–1401.

Sánchez-Alfaro, P., Reich, M., Driesner, T., Cembrano, J., Arancibia, G., Pérez-Flores, P., Heinrich, C., Rowland, J., Tardani, D., Lange, D., Campos, E., 2016a. The optimal windows for seismically-enhanced gold precipitation in the epithermal environment. Ore Geol. Rev. 79, 463–473.

Sánchez-Alfaro, P., Reich, M., Arancibia, G., Pérez-Flores, P., Cembrano, J., Driesner, T., Lizama, M., Rowland, J., Morata, D., Heinrich, C.A., Tardani, D., Campos, E., 2016b. Physical, chemical and mineralogical evolution of the Tolhuaca geothermal system, southern Andes, Chile: insights into the interplay between hydrothermal alteration and brittle deformation. J. Volcanol. Geotherm. Res. 324, 88–104.

Shaw, D., Sturchio, N., 1992. Boron-lithium relationships in rhyolites and associated thermal waters of young silicic calderas, with comments on incompatible element behavior. Geochim. Cosmochim. Acta 56, 3723–3731.

Sibson, R., 1996. Structural permeability of fluid-driven fault-fracture meshes. J. Struct. Geol. 18, 1031–1042.

Simmons, S., Browne, P., 2000. Hydrothermal minerals and precious metals in the sulfidation epithermal environments. Econ. Geol. 95, 971–999.

Somoza, R., 1998. Updated Nazca (Farallón)-South America relative motions during the last 40My: implications for the mountain building in the central Andean region. J. S. Am. Earth Sci. 11, 211–215.

Sturchio, N., Muhlenbachs, K., Seitz, M., 1986. Element redistribution during hydrothermal alteration of rhyolite in an active geothermal system: Yellowstone drill cores Y-7 and Y-8. Geochim. Cosmochim. Acta 50, 859–872.

Tardani, D., Reich, M., Roulleau, E., Takahata, N., Sano, Y., Pérez-Flores, P., Sánchez-Alfaro, P., Cembrano, J., Arancibia, G., 2016. Exploring the structural controls on helium, nitrogen and carbon isotope signatures in hydrothermal fluids along an intra-arc fault system. Geochim. Cosmochim. Acta 184, 193–211.

Tardani, D., Reich, M., Deditius, A.P., Chryssoulis, S., Sánchez-Alfaro, P., Wrage, J., 2017. Cu-as decoupling in an active geothermal system: a link between pyrite and fluid composition. Geochim. Cosmochim. Acta 204, 179–204.

Tassara, A., Yáñez, G., 2003. Relación entre el espesor elástico de la litósfera y la segmentación tectónica del margen andino (15–47˚S). Rev. Geol. Chile 30, 159–186.

White, D., 1957. Thermal waters of volcanic origin. Bull. Geol. Soc. Am. 68, 1637–1658.